Monitoring of service life consumption for tubular solar receivers: Review of contemporary thermomechanical and damage modeling approaches

D. Hering[a,*], M. Binder[b], P. Schwarzbözl[a], R. Schwaiger[c], R. Pitz-Paal[a]

[a] *Institute of Solar Research, German Aerospace Center, Linder Hoehe, 51147 Koeln, Germany*
[b] *MAN Energy Solutions SE, New Technologies, Werftstraße 17, 94469 Deggendorf, Germany*
[c] *Institute of Energy and Climate Research (IEK), Forschungszentrum Juelich, 52425 Juelich, Germany*

Abstract

Concentrating solar power plays a vital role in the transformation of global energy landscape towards sustainable and environmentally sound energy supply. Currently, tower systems with molten salt tubular receivers are most common in commercial scale applications. Operational optimization of such systems necessitates detailed knowledge of operating limits of receiver components exposed to inhomogeneous solar flux densities of up to 1 MW/m^2 and local salt temperatures of in part more than 600 °C, fluctuating at various time scales. Traditionally, the operating limits aforementioned are captured in a simplified manner via the top-down concept of allowable flux density. To the authors' view, there is considerable room for improvement over this approach as far as optimization of inherent thermomechanical and damage modeling are concerned. What is more, an alternative bottom-up concept, though implying more stringent requirements on model and processing performance, promises notably increased economic viability essentially due to reduced safety margins in operation and condition-based maintenance strategies. In this paper, essential approaches and assumptions of thermomechanical and damage modeling meth-

*Corresponding author
Email address: dominik.hering@dlr.de (D. Hering)

ods in topical literature are comprehensively discussed and assessed in terms of their potential for the approach outlined to be demonstrated at a pilot scale test facility. As a result, it is concluded that modeling can be substantially improved applying extended analytical methods from the literature. In addition, depending on model complexity and available computational resources, a few heuristic-numerical models are potentially applicable in favor of more detailed thermomechanical modeling regarding i.a. actual receiver geometry and local boundary conditions.

Keywords: molten salt solar tubular receiver, operational optimization, allowable flux density, thermal stress, creep-fatigue damage, corrosion

1. Introduction

Nowadays, mitigation of climate change – essentially tantamount to a quick and substantial reduction of global greenhouse gas emissions – is one of the most fundamental challenges humankind faces. Increasing the share of renewable energy resources in energy consumption is a central element of respective solution strategies (e.g. IRENA (2019)). In this context, dispatchable electricity and heat generation by concentrating solar power (CSP) technologies is considered an effective and increasingly competitive option for regions with sufficiently high solar energy potential (Lilliestam et al., 2020; Pitz-Paal, 2020).

Currently, tower systems with external tubular receiver configurations are most common in commercial scale applications (cf. Fig. 1), a major part utilizing molten salts such as Solar Salt – an eutectic mixture of sodium and potassium nitrate (Conroy et al., 2018c) – as heat transfer and storage medium (Conroy et al., 2020; Fritsch et al., 2017; Qiu et al., 2019).

Optimization of such a system from a thermodynamic viewpoint requires detailed knowledge of operating limits regarding reliability and service life of receiver components exposed to inhomogeneous solar flux densities up to 1 MW/m^2 and local salt temperatures of in part more than 600 °C, fluctuating at various time scales due to immanently transient character of solar radiation, cloud

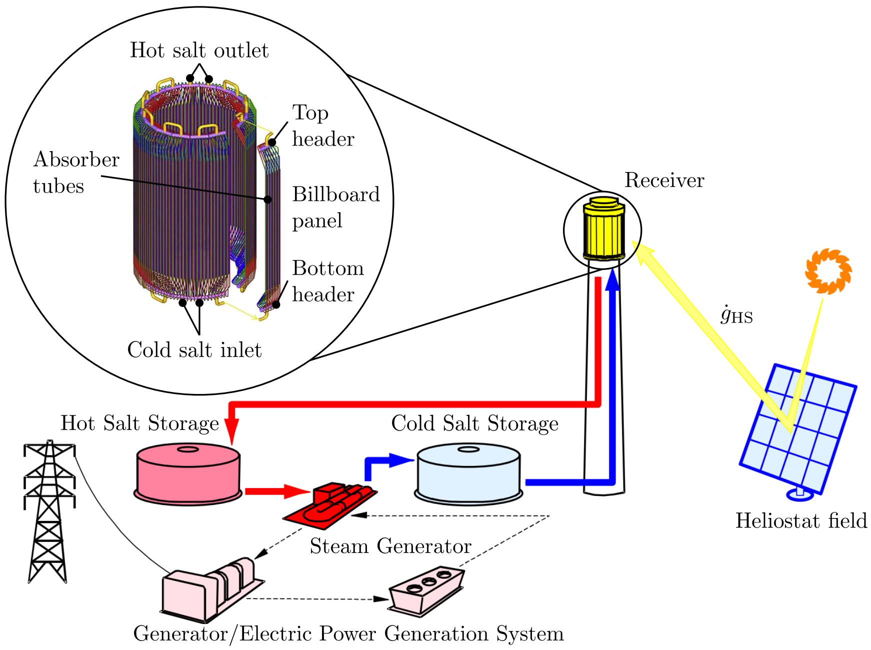

Figure 1: Schematic of molten salt CSP tower system and respective design of tubular receiver by the example of an external cylindrical configuration (cf. Pacheco (2002); Rodríguez-Sánchez et al. (2014b)): The billboard-shaped panels consist of an array of absorber tubes joined by top and bottom header and can be interconnected in various ways; here, the cold salt entering the receiver at the inlet meanders through two parallel paths in serpentine flow

passage, daily startup and shutdown, wind dependent convective losses etc. (González-Gómez et al., 2021; Vant-Hull, 2002).

Traditionally, the operating limits aforementioned are captured in a simplified manner via the concept of allowable flux density (AFD), originally introduced by Kistler (1987) following a methodology described in Babcock and Wilcox Company (1984). Smith (1992) employs the analytical model in Kistler (1987) for the calculation of thermoelastic strain at the irradiated tube crown in order to derive an implicit expression for the AFD as a function of salt bulk temperature and velocity. Thereby, he assumes one-dimensional heat transfer and approximates the resulting strain $\varepsilon_{\mathrm{eq}}$ at tube crown as the sum of strain due to radial temperature difference at the crown and average circumferential – front-to-back – temperature difference (cf. Young and Budynas (2002))[1]. The corresponding admissible strain ranges $\Delta\varepsilon_{\mathrm{adm,f}}$ are derived using measurement-based, extrapolated direct-normal insolation (DNI) cycles grouped by range from Kistler (1987)[2] and isothermal fatigue data taken from ASME (1980), Code-Case (CC) N-47 applying linear damage rule for fatigue cycles. Vant-Hull (2002) presents an explicit polynomial fit of the AFD-formulation in Smith (1992) taking into account corrosive nature of molten salt at elevated temperatures by restriction of local film temperatures. The difference between computationally determined absorbed flux density and AFD – derived from measured salt temperature increase between in- and outlet – enabled detection of local excess flux and subsequent adjustment of individual heliostat aimpoints during operation of the pilot plant Solar Two.

To the authors' view, there is considerable room for improvement over the traditional (top-down) AFD-concept as described before concerning three major aspects:

[1] Here, Kistler (1987) additionally suggests both an empirical correlation for consideration of further directional strain components in equivalent strain calculation and a correction factor of 1.1 adopted from Narayanan et al. (1985) to account for plastic strain effects.

[2] In Kistler (1987), the insolation cycles are tabulated depending on minimum and maximum values, i.e. cycle range and mean value, the influence of latter being neglected in Smith (1992).

(i) Though practicable, the derivation of admissible strain ranges based upon forecast insolation cycles on the one hand neglects transient/short-term fluctuations attributed to cloud passages etc. (see above) – thus necessitating additional adjustment of local flux distribution at off-nominal conditions (Vant-Hull, 2002). On the other hand, a more flexible operation e.g. allowing for intentionally disproportionate service life consumption in favor of thermodynamic efficiency in certain load situations is desirable enabling the implementation of holistic system optimization by contemporary control concepts. Therefore, in the context of operational optimization, a bottom-up approach modeling the local receiver state depending on current thermomechanical boundary conditions and cumulating the service life consumption over time[3] seems beneficial[4], basically also paving the way to more situative and cost-effective, condition-based maintenance strategies[5].

(ii) The analytical model for the calculation of local thermoelastic strain as given in Smith (1992) is straightforward, real-time capable and thus directly applicable within the outlined bottom-up approach, however it incorporates numerous simplifications and requires careful revision for consideration of actual local load states of a complete three-dimensional receiver geometry under diverse boundary conditions.

(iii) ASME (1980), CC N-47, which was originally developed for design of nuclear reactors and applied to solar receivers for lack of alternatives, implies

[3]It should not go unmentioned that a bottom-up approach as described here was already implemented in principle by Grossmann et al. (1989) relying on the findings of Babcock and Wilcox Company (1984). The local receiver state over time was approximated with measurement-based determination of local salt bulk temperature, flow and flux. Subsequently, the fatigue cycles were counted using filtering and rainflow algorithm techniques from Downing and Socie (1982).

[4]Notwithstanding the above, in other contexts, such as initial design and optimization of receiver or heliostat field, the top-down AFD-concept obviously still has relevant application possibilities.

[5]As an aside, it is noteworthy that condition-based monitoring, control and maintenance is generally seen as an increasingly relevant research field even on energy system level i.a. owing to partly outdated design methods inappropriate for modern, highly dynamic load states of system components (BDEW, 2020).

a considerable level of conservativity while simultaneously – in its modified form used for AFD-calculation as given above – neglecting both effects of (cyclic) plastic strain in fatigue damage and creep damage as well as creep-fatigue damage interaction (cf. Sec. 3 for more recent literature, where, for the most part, creep damage and creep-fatigue damage interaction is accounted for).

In this paper, essential approaches and assumptions of modeling methods in topical literature – relevant to the subject outlined beforehand, however, to the authors' knowledge so far mainly applied at design stage or in conceptual studies – are presented in detail. For the sake of clarity, the results are categorized as either dealing with (numerical, analytical) thermomechanical (Sec. 2) or damage modeling (Sec. 3).

Subsequently, the paper concludes with a brief summary of approaches and an assessment of their applicability regarding consideration of service life consumption in operational optimization as well as exploitation of identified potential for improvement (i)-(iii).

2. Thermomechanical modeling

2.1. Overview

Calculation of local quasi-static stress $\boldsymbol{\sigma}(\mathbf{x}, t)$ as given in Eq. (1) as well as corresponding strain $\boldsymbol{\varepsilon}(\mathbf{x}, t)$ is generally dependent on constitutive material model, thereby i.a. temperature distribution $T(\mathbf{x}, t)$, body forces due to gravity $\mathbf{g}$ and external constraints, i.e. mechanical boundary conditions at inner and outer boundaries of solid domain. Temperature distribution $T(\mathbf{x}, t)$ as in Eq. (2), in turn, essentially depends on thermal boundary conditions at inner and outer boundaries of solid domain (Eslami et al., 2013; Willner, 2003; Young and Budynas, 2002).

$$0 = \nabla \cdot \boldsymbol{\sigma} + \rho \mathbf{g} \tag{1}$$

$$\rho c \frac{\partial T}{\partial t} = \nabla \cdot (K \nabla T) \tag{2}$$

The dependence on boundary conditions at solid domain boundaries is illustrated in Fig. 2 for an arbitrarily discretized tube segment, omitting the influence of support structure (clips, bearings etc.) for simplicity.

First, within thermal modeling as depicted in the upper left of Fig. 2, at the inner boundary the convective heat flux from solid to fluid $\dot{q}^{\mathrm{i,C}}$ has to be appropriately modeled on local level. At the outer boundary, both (natural, forced) convective thermal losses to surroundings $\dot{q}^{\mathrm{o,C}}$ and radiative heat exchange $\dot{q}^{\mathrm{o,R}}$ have to be taken into account[6], the latter being composed of heat exchange due to differing surface temperatures $T_1^{\mathrm{o}}, ..., T_m^{\mathrm{o}}$ of involved components or rather elements and heat exchange due to solar irradiation $\dot{g}_{\mathrm{HS}}$ from heliostats.

Second, local stress and strain within the mechanical model (cf. bottom right of Fig. 2) can be calculated based upon corresponding temperature distribution and additional influence factors. Besides constraints due to support structure, these comprise volumetric effects due to gravity $\mathbf{g}$ and distributed forces at domain boundaries $\nabla \cdot \boldsymbol{\sigma} \cdot \mathbf{e}^{\mathrm{i}}$, $\nabla \cdot \boldsymbol{\sigma} \cdot \mathbf{e}^{\mathrm{o}}$ due to internal (fluid) and external pressure.

2.2. Thermomechanical modeling methods applied in literature

Based upon the brief overview given in the previous section, essential results of a review on topical literature detailing the respective methodology for calculation of local stresses and strains are presented in Sec. 2.2.1 (regarding numerical methods) and Sec. 2.2.2 (regarding analytical methods). An overview of both numerical and analytical approaches is given in Appendix A, further

[6]Conductive heat losses in particular due to support structure and insulation in direct contact with tubes can be typically neglected (e.g. Conroy et al. (2020)).

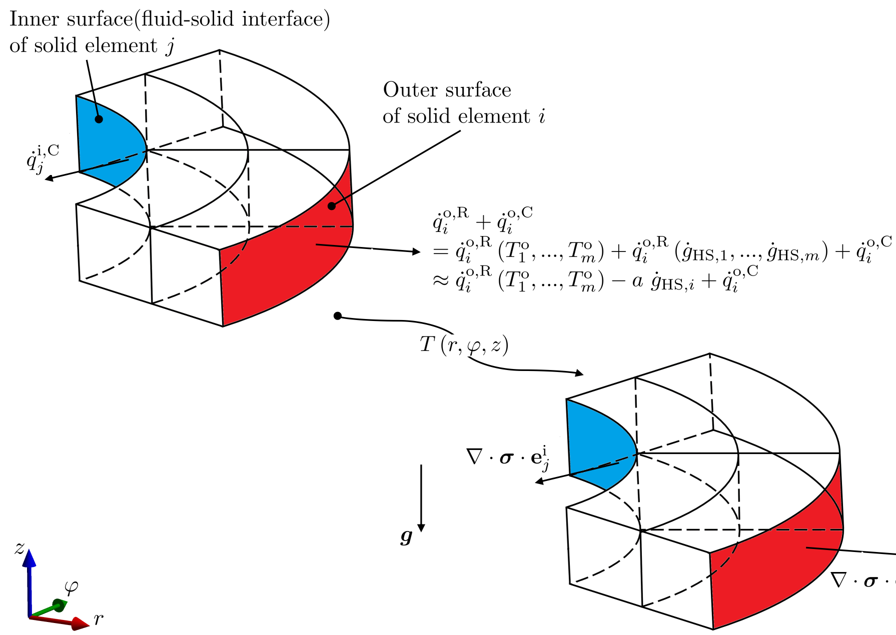

Figure 2: Schematic sketch of external thermal (upper left) and mechanical (bottom right) boundary conditions for solid elements i, j of an arbitrarily discretized tube segment, inner surface of element j in blue, outer surface of element i in red

broken down by thermal (Tab. A.1 and Tab. A.3) and mechanical modeling methods (Tab. A.2 and Tab. A.4).

2.2.1. Numerical methods

Fork et al. (2012) examines thermal stress and creep-fatigue damage for an internal tubular receiver system made of alloy 617 considering both thermal and pressure induced loads based upon previous work. For the mechanical model, temperature dependent material properties and effects of plastic strain/stress relaxation due to secondary creep are taken into account. Secondary (equilibrium) creep rates are modeled based on Norton power law and Arrhenius rate, both explicitly and as an alternative, relying on stress relaxation data[7]. Due to performance reasons, however, the nonlinear numerical model is restricted to a representative, two-dimensional (2D) tube segment discretized with one element in axial and 20 elements in radial direction.

Yang et al. (2012) studies the characteristics of steady-state conjugate heat transfer (CHT) for HITEC salt flow in a single receiver tube (alloy 625) under circumferentially inhomogeneous heating both numerically and experimentally. For the three-dimensional (3D) computational fluid dynamics (CFD) analysis, Reynolds averaged Navier-Stokes (RANS) equations with k-ε turbulence model considering temperature dependence of properties $\overline{\overline{\rho}}$, $\overline{\overline{\mu}}$ are applied. A comparison of numerically and experimentally determined mean Nusselt numbers N_{Nu} shows good agreement with deviations of ± 7.5 % for $N_{\mathrm{Re}} \in \left\{10^4, 4 \cdot 10^4\right\}$. Although only weak dependences of circumferential angle on local N_{Nu} are discerned, Sieder-Tate correlation is considered not suitable for calculation of average heat transfer because of locally large temperature differences between tube wall and salt due to inhomogeneous heating[8].

[7] It should be noted that at temperatures up to 1300 K of air used as heat transfer fluid (HTF), conditions and significance of creep damage as discussed in Fork et al. (2012) are different from those in molten salt-based systems.

[8] Compare Ying et al. (2020), where an analog approach is chosen to examine molten salt-based nanofluid as HTF under both circumferentially and axially non-uniform heating. Simulation results for pure HITEC salt show maximum deviations of ± 12.5 % for Gaussian-cosine type flux boundary condition regarding mean Nusselt numbers N_{Nu}, calculated with

In a similar analysis carried out by Chang et al. (2014), Dittus-Boelter correlation is considered appropriate for calculation of average heat transfer under circumferentially inhomogeneous heating, however, using water as HTF and assuming constant properties as well as incompressible flow. Additionally, for local wall temperature distribution, a CFD-based regression formula is presented.

Flores et al. (2014) studies steady-state-CHT and linear-thermoelastic stress for HITEC salt flow in a circular pipe subjected to inhomogeneous heating in circumferential direction. In contrast to Yang et al. (2012) et al., assuming fully developed flow and constant material properties for simplicity, CHT is analyzed using a 2D formulation for the Reynolds averaged cross-plane temperature fluctuations and a spectral solution method based upon analytical expressions for Reynolds averaged axial velocity $\widehat{v}_z(r)$, turbulent eddy viscosity $\mu^T(r)$ and conductivity $K^T(r)$ from Cess (1958).

In favor of reduced model complexity and consequently computational effort for modeling on panel or receiver level, Rodríguez-Sánchez et al. (2014b) presents two novel modeling approaches and corresponding numerical solution schemes for steady-state CHT of external receiver absorber tubes (alloy 800H) with Solar Salt as HTF. In both approaches, the tube shell is discretized in axial and circumferential direction, correspondingly, temperature is assumed to vary in axial and circumferential direction. In the homogeneous temperature model, homogeneous temperature is assumed within a discrete cell of the tube shell, whereas in the homogeneous heat flux model, homogeneous heat flux absorbed by a discrete cell is assumed. Calculation of radiation exchange $\dot{q}_i^{\mathrm{o,R}}$ at outer surface of element i is modeled between outer tube surfaces, backside (refractory wall) and surroundings via net radiation method (cf. Bergmann et al. (2011)), including solar irradation $\dot{q}_i^{\mathrm{o,R}}(\dot{g}_{\mathrm{HS},1}, ..., \dot{g}_{\mathrm{HS},m})$ from heliostats at design point. Herein, radiative properties are taken from Slemp and Wade (1962); Zavoico (2001)[9]. As the absorber tubes are axially discretized into segments of length

the numerical model and, alternatively, with Gnielinski correlation.

[9]As a side remark, application of net radiation method as given in Rodríguez-Sánchez et al. (2014b) provides $\epsilon_i = a_i$, i.e. consideration of solar irradiation within $\dot{q}_i^{\mathrm{o,R}}$ in Rodríguez-

Δz being on the one hand sufficiently small for justifiying the assumption of homogeneous surface temperatures, on the other hand, however, large enough for neglection of radiation exchange between axially displaced elements, 2D view factors are determined with Crossed-Strings method as given in Modest (2003). Equivalent temperature of the surroundings is calculated according to Berger et al. (1984). Additionally, both natural and forced convective thermal losses to the surroundings $\dot{q}_i^{\mathrm{o,C}}$ are captured using a correlation for the external heat transfer coefficient from Siebers and Kraabel (1984). Conduction inside the tube walls is only considered in radial direction, taking into account temperature dependence for thermal conductivity of tubes K. The fluid enthalpy flow is modeled with a one-dimensional (1D) approach with temperature dependent properties $\overline{\overline{\rho}}$, $\overline{\overline{\mu}}$, c_p and $\overline{\overline{\overline{K}}}$ according to Zavoico (2001). In an additional 3D CFD model of representative panel tubes used for validation purposes, the fluid flow inside the tubes is modeled applying RANS-equations and k-ε turbulence model in conjunction with enhanced wall treatment; radiative heat exchange is modeled choosing the Discrete Ordinate model. Comparisons of external tube wall temperature profiles in axial and circumferential direction for various angles and heights, respectively, reveal maximum local differences of 2.5 % between homogeneous temperature and CFD model. Similarly, for various mass flows rates and wind velocities evaluated, outlet salt and maximum external tube wall temperatures deviate by a maximum of 7.5 % and 2.5 %, respectively. Maximum difference for circumferentially averaged, absorbed heat flux is specified as less than 6 %.

In Rodríguez-Sánchez et al. (2018), the approach from Rodríguez-Sánchez et al. (2014b) is extended focusing on improved modeling of radiative heat exchange on individual tube level and thus better approximation of (maximum)

Sánchez et al. (2014b) formally prohibits usage of emissivity in infrared spectrum and absorptivity in visible spectrum herein. As an alternative, the iterative matrix method presented in Laporte-Azcué et al. (2020b) is applicable instead. Simplifying, the influence of solar irradiation can also be neglected in terms of radiation exchange in favor of using absorptivity in visible spectrum by directly introducing absorbed solar irradiation $\dot{g}_{\mathrm{HS},i}^{\mathrm{abs}} = a_i \; \dot{g}_{\mathrm{HS},i}$ in local thermal balance, as others suggest (see below, also compare Fig. 2).

tube wall temperature, generally adopting temperature dependent properties for tube material (alloy 625) and Gnielinski correlation for N_{Nu} from Gnielinski (2013).

Zhang et al. (2015) proposes and experimentally validates a transient thermal model for an internal tubular receiver with molten salt as HTF. Temperature dependent material properties are applied throughout. Similar to Rodríguez-Sánchez et al. (2014b), conduction inside the tubes axially divided into annular segments is only considered in radial direction, fluid pressure loss and enthalpy flow is described with a 1D model using Colebrook-White equation from Colebrook (1939) for f and Gnielinski correlation from Gnielinski (1976) for N_{Nu}. Radiative heat exchange $\dot{q}_i^{\mathrm{o,R}}$ between outer tube, inner cavity and aperture surfaces is taken into account via net radiation method with uniform radiative properties, admitting temperature dependence of ϵ for the tube surfaces. View factors are determined with Monte-Carlo method. Convective thermal losses $\dot{q}_i^{\mathrm{o,C}}$ are captured combining correlations for natural heat transfer coefficient from Siebers and Kraabel (1984) and forced heat transfer coefficient for a vertical plate (cf. Li et al. (2010)). The comparison of outlet temperatures between numerical model and experimental setup for various mass flow rates, inlet temperatures and input power (heat) showed deviations of less than 3 % under steady-state conditions, whereas somewhat higher deviations occur in transient regime, indicating i.a. sensitivity of the numerical model to flow rate variations.

Du et al. (2016) examines fatigue fracture of an irradiated tube segment made of 316H stainless steel due to thermally induced mechanical loads. For the 3D thermal model basically analogous to Rodríguez-Sánchez et al. (2014b); Yang et al. (2012), an axially varying incident solar flux obeying normal distribution and temperature dependent properties for solar salt according to Dunn et al. (2012) are assumed.

Doupis et al. (2016) investigates transient operation modes and structural integrity of a Solar Salt tubular receiver system. For the latter, a 3D transient thermal model limited to the outlet header region is developed. Local salt bulk temperatures are prescribed based upon previous work, corresponding heat transfer coefficients are modeled with Dittus-Boelter equation multiplied with segmentally averaged enhanced turbulence factors extracted from a 3D-CHT parametric study. Within the mechanical model, both thermal and internal pressure loads are considered.

Ortega et al. (2016a) explores candidate materials and tube sizes for a tubular receiver with pressurized sCO_2. Based upon a preliminary design configuration with alloy 625 as tube material and results from Ortega et al. (2016b), a linear-elastic 3D mechanical model of a representative tube section considering both thermal and pressure loads is set up and, subsequently, a creep-fatigue damage analysis is performed.

In a parameter study, Marugán-Cruz et al. (2016) compares local heat fluxes, temperatures and linear-thermoelastic stresses for a 2D tube segment exposed to sinusoidal heat flux at the irradiated half shell for two different modeling approaches. The detailed thermal model is chosen in accordance with Flores et al. (2014) whereas in a simplified 1D model, inside the tube only conduction in radial direction is accounted for. Furthermore, the fluid enthalpy flow is modeled using an explicit formulation for f in line with Petukhov (1970) and Gnielinski correlation taken from Gnielinski (1976). For the various cases studied, the deviations in local heat flux at the inner tube wall obtained with the 1D model increase with decreasing Biot number N_{Bi} as defined in Marugán-Cruz et al. (2016). For an accurate film temperature prediction with an error of less than 5 % compared to the 2D approach, $N_{\mathrm{Bi}} \gtrsim 0.3$ is derived as a rule of thumb.

Nithyanandam and Pitchumani (2016) investigates the performance of external tubular receiver systems with sCO_2 as HTF analyzing creep-fatigue damage for various operating points and designs. In the thermal 2D model, temperature dependence of respective properties for fluid and tube material (alloy 230) is considered. Conduction inside the tube walls is – different from Rodríguez-Sánchez et al. (2014b) et al. – accounted for in radial and axial direction. Simplifying, however, axisymmetric temperature distribution both in solid and fluid domain is assumed[10], resolving the latter in radial and axial direction applying RANS-equations and k-ε turbulence model. Radiative heat exchange $\dot{q}_i^{\mathrm{o,R}}$ between outer tube wall and surroundings is modeled with $\epsilon = 0.88$, while solar absorptivity a is equated to 0.95 according to Ho et al. (2013); regarding convective losses $\dot{q}_i^{\mathrm{o,C}}$, a baseline heat transfer coefficient of 10 $\mathrm{W/m^2\,K}$ taken from Ho and Iverson (2014) is assumed.

Flesch et al. (2017) presents a dynamic thermal model approach for irradiated molten salt receiver tubes studying transient operation during cloud passage and corresponding incident solar flux maps determined by ray-tracing. The tube walls are divided into front and back shell and additionally discretized in axial direction. At the outer shell surfaces, both radiative heat exchange and convective heat losses are considered. The fluid domain is captured with a modular 1D approach principally equivalent to Zhang et al. (2015), moreover being basically capable of simulating two-phase flow conditions. A 3D CFD model for validation purposes is set up in accordance with Du et al. (2016) et al., showing good agreement of salt bulk temperature distribution in a steady-state reference case. Circumferential variation of tube wall temperatures obtained with the CFD model, however, cannot be precisely reproduced owing to coarse discretization of the tube into front and back shell. In an additional, dynamic load case with varying mass flow rate and incident flux, again, fluid temperatures agree well with experimental data.

In Fritsch et al. (2017) – besides examination of heat transfer characteristics of liquid metals in the context of tubular solar receivers – a 3D transient thermal model for an absorber tube (316H stainless steel) of an external receiver with Solar Salt as HTF is presented. The 3D solid domain discretized with one element in radial direction is coupled with a 1D enthalpy flow model considering temperature dependent properties of solar salt from Zavoico (2001). N_{Nu} is modeled using Gnielinski correlation together with an explicit form for f

[10] See below, Sec. 2.2.2 and herein, especially Marugán-Cruz et al. (2016) regarding validity of this assumption.

according to Verein Deutscher Ingenieure, VDI-Gesellschaft Verfahrenstechnik und Chemieingenieurwesen (2010). For validation of the single tube model which in principle is also employed in the framework of the modular Advanced Solar Tubular ReceIver Design (ASTRID©) tool (Frantz et al., 2017), a detailed 3D CFD model solving RANS equations inside the fluid domain is applied. Herein, Reynolds stresses are modeled using k-ω-SST approach together with Reynolds analogy for corresponding turbulent heat transfer. Buoyancy is accounted for using Boussinesq approximation. Both in a steady-state load case and a transient case with variable flux, the single tube model reproduces the results of the detailed CFD model sufficiently well, with maximum deviations in tube wall front temperature at the inlet attributed to developing flow going along with lower wall temperatures in the CFD model. On panel level, in favor of reduced computational effort, besides the application of the single tube model, which enables accounting for radiative heat exchange between outer tube surfaces, backwall insulation and surroundings, a simplified quasi-1D model where the irradiated tubes walls are treated as projected surfaces, therefore only considering radiative heat exchange of planar tube surfaces with surroundings, is analyzed. In light of significant deviations in particular regarding radiation losses and restrictions with respect to modeling of incident flux, however, the simplified approach is not recommended for further investigation. Thus, the more detailed model is applied within a receiver simulation of Solar Two investigating various wind speeds at a representative incident flux distribution. Herein, radiative properties are taken from Pacheco (2002). Additionally, convective thermal losses are taken into account, using heat transfer coefficients from a CFD study (compare Uhlig et al. (2016); Zanino et al. (2014)).

In a study focusing on thermohydraulic performance of various HTFs for application in tubular receiver systems, Conroy et al. (2018c) in principle follows the approach of Rodríguez-Sánchez et al. (2014b). Conduction is only accounted for in radial direction inside the walls of an alloy 800H tube discretized in axial and circumferential elements. As before, for 1D enthalpy flow and pressure loss, correlations for f and N_{Nu} are taken from Petukhov (1970) and Gnielinski

(1976). Calculation of radiation exchange $\dot{q}_i^{\mathrm{o,R}}$ is taken into account between outer tube wall and surroundings with temperature dependent ϵ, absorptivity a is introduced as function of irradiance incident angle (Ho et al., 2013). As in Rodríguez-Sánchez et al. (2014b), view factors are determined with Crossed-Strings method. Convective thermal losses to surroundings $\dot{q}_i^{\mathrm{o,C}}$ are modeled with correlations for natural, forced and total heat transfer coefficient (see above and Siebers and Kraabel (1984)).

In Conroy et al. (2018a,b), the approach is extended to a linear-elastic mechanical and creep-fatigue damage analysis for investigations on a variety of aiming strategy and receiver panel configurations as well as tube materials, with liquid sodium as HTF. Here, within the thermal model, heat transfer at the inner tube walls is modeled with an analytical correlation from Gärtner et al. (1974) applicable for azimuthally inhomogeneous heat flux boundary conditions that can be represented by a Fourier series expression.

In Logie et al. (2018), a numerical-analytical solution method to steady-state CHT and linear-elastic stress for non-axisymmetrically heated tubes is applied in a comparative study of Solar Salt and liquid sodium as HTF. The temperature profile inside the tube made of stainless steel 316 is derived from 2D Laplace equation in cylindrical coordinates assuming axial symmetry and using Gauss-Seidel iterative method. At the outer boundary of the tube domain, both radiative heat exchange between tube segment and surroundings with $\epsilon = 0.87$ (Ho et al., 2013) and convective thermal losses with a reference heat transfer coefficient of 30 W/m^2 K accounting for considerable wind are considered (cf. Siebers and Kraabel (1984)). For determination of absorbed solar irradiation, a is approximated with 0.97. Fluid enthalpy flow is modeled similar to Rodríguez-Sánchez et al. (2014b) et al. with Dittus-Boelter equation (cf. Bergmann et al. (2011)) for N_{Nu} of Solar Salt.

Subsequently, in Montoya et al. (2018) a 3D linear-thermoelastic analysis of a Gemasolar-like alloy 800H receiver panel with Solar Salt is performed employing both a numerical and a simplified analytical approach. Thermally induced loads are obtained based upon Rodríguez-Sánchez et al. (2014b), temperature dependent E, ν and α are adopted for the numerical model. In order to save computational resources, except for a small section where the maximum temperature is located, the wall of the representative tube modeled is discretized with 2D shell elements. A comparison of thermal stress components from the numerical model with those obtained with the analytical approach adopted from Logie et al. (2018) (see below, Sec. 2.2.2) reveals only moderate deviations along the outer tube wall perimeter, evaluated at the point of maximum temperature.

Relying on the ASTRID© tool (see above) for simulation of temperature profiles within absorber tubes, Uhlig et al. (2018) carries out a 3D linear-elastic mechanical analysis for a representative panel of the Solar Two receiver, including header and connection tubes. In addition to thermally induced stress, gravity and pressure effects are taken into account. Sub modeling technique is applied for detailed resolving of regions with maximum stress. The temperature field inside the header and connection tube walls is approximated applying a forced convection boundary condition at the inside with representative heat transfer coefficient and fluid temperature (compare Doupis et al. (2016); Frantz et al. (2020)). Besides solar operation, a separate analysis using a transient thermal, solid model for simulation of local load states during filling is performed.

In a scenario analysis on thermal performance of tubular solar receivers, Xu et al. (2018) develops a 3D transient model for the absorber tube wall based upon geometry and material data from Sánchez-González et al. (2017). Both radiative heat exchange between outer tube wall and surroundings with $\epsilon = 0.87$ as well as convective thermal losses are considered. Absorptivity a is given by 0.93 (Zavoico, 2001). For modeling of convective thermal losses, correlations for natural, forced and total heat transfer coefficient are applied as given in Siebers and Kraabel (1984). Fluid enthalpy flow is modeled similar to Fritsch et al. (2017), with salt properties as given in Benoit et al. (2016) and correlations for f and N_{Nu} taken from Petukhov (1970), Bergmann et al. (2011), respectively.

Barua et al. (2019) evaluates various ratcheting and creep-fatigue design approaches of ASME Boiler and Pressure Vessel Code, Section III, Division 5 (ASME BPVC-III-5) (ASME, 2017) for a reference gen3 tubular receiver with an eutectic mixture of $MgCl_2$-KCl as HTF. For the underlying thermal-structural analysis, two representative tubes made of alloy 740H are selected, considering temperature dependent material properties throughout. Within the steady-state thermal model, salt bulk temperature is assumed to increase linearly in flow direction, with predefined inlet and outlet temperatures and appropriate heat transfer coefficients. Both radiation exchange between tubes and surroundings and convective thermal losses are considered at determined design point. For the nonlinear/inelastic mechanical model, plastic strain effects are captured assuming J_2-plasticity in conjunction with Voce hardening model, creep is taken into account via a power law approach by analogy with Fork et al. (2012)[11].

Qiu et al. (2019) studies flow friction and heat transfer characteristics of turbulent pipe flow for various molten salts both numerically and experimentally. Within the 3D CFD absorber tube model, temperature dependent salt properties are considered. RANS equations in the fluid domain are applied using k-ε-model and Reynolds analogy. In the near-wall region, velocity and temperature gradients are modeled with logarithmic wall functions. Simulations of average wall friction and heat transfer characteristics under representative, uniform and non-uniform incident flux at various fluid temperatures and Reynolds numbers N_{Re} revealed no significant differences, suggesting general applicability of correlations for uniform boundary conditions. For average wall friction, Filonenko correlation is proposed with maximum deviations of ± 2 % compared to numerical results with uniform incident flux. Regarding average heat transfer, Sieder-Tate and Gnielinski correlation are found to be appropriate, with maximum deviations of about ± 15 %. As an alternative, a modified correlation for mean Nusselt number N_{Nu} is given resulting in less than ± 5 % relative error for the data points simulated[12].

[11] Compare also Frantz et al. (2020), where, in the context of a creep-fatigue evaluation for a prototypic molten salt high temperature receiver at design stage, following ASME BPVC-III-5 as well, a nonlinear Chaboche model is combined with a Norton-Bailey power law approach for the absorber tubes made of austenitic alloy DMV 310N.

[12] Summarizing key findings collected in this section with respect to 1D fluid models extensively used in literature, it can be concluded that application of common friction factor and Nusselt number correlations for molten salt receiver tubes with inhomogeneous incident solar

Recently, in Rao et al. (2021), an AFD-study is performed for an internal, coiled tube receiver with sCO_2 studying the influence of various flux distributions and HTF parameters at tube inlet. The 3D solid domain is coupled with a steady-state 1D enthalpy flow model, whereby heat transfer is modeled with Gnielinski correlation from Gnielinski (1976) and an explicit form of f multiplied by a correction factor for spiral tubes. Both radiation exchange between outer tube, inner cavity (insulation) and aperture surfaces and convective thermal losses are considered. Resulting temperature profiles provide boundary conditions for the subsequent calculation of resulting linear-thermoelastic stresses and strains, assuming constant properties of alloy 230 selected as tube material.

2.2.2. Analytical methods

Irfan and Chapman (2009) summarizes a variety of analytical methods for calculation of linear-elastic stress in irradiated tubes due to directional temperature gradients. Under an arbitrary axial temperature gradient, i.e. $T = T(z)$, the series solution to normal and shear stress components as given in Lee (1966), leaving aside end effects and assuming traction-free outer and inner shell surfaces, is presented. As further mentioned, in Yang and Lee (1971), this solution is extended to radially and axially varying temperature $T = T(r, z)$ expressible in the form $T(r, z) = \sum_{n=0}^{N} \left(r - \left(r^{\mathrm{i}} + r^{\mathrm{o}}\right)/2\right)^n \; T_n(z)$. For temperature distributions varying in radial and circumferential direction $T = T(r, \varphi)$, superimposable expressions for resulting hoop stress assuming 2D thermoelasticity are presented according to Goodier (1957); Young and Budynas (2002)[13]. For hoop

---

flux seems generally reasonable. Nevertheless, their effects on locally resolved tube temperature (gradients) throughout the solid domain and, in turn, on local thermal stresses should be preferably individually checked. What is more, implicit neglection of effects of developing flow on local fluid flow, heat transfer and thermal stresses has not been exhaustively studied so far, so particular care should be taken when modeling complex, curved 3D tube geometries (see e.g. Doupis et al. (2016); Rao et al. (2021); Uhlig et al. (2018)).

[13]For a complete representation of resulting stress components imposing simple plane strain condition it is referred to e.g. Marugán-Cruz et al. (2016).

Logie et al. (2018) moreover elaborates on approximation of axial stress assuming zero axial force, generalized plane strain or, alternatively, zero axial force with annulled bending moment. In addition, Logie et al. (2018) exemplarily compares equivalent thermal stress at stress due to circumferentially varying part $T_\varphi(r,\varphi)$, coefficients of the Fourier transform of $T(r,\varphi)$ for axial symmetry at the inner and outer tube radius are introduced neglecting higher harmonics and remaining linear terms[14].

Flores et al. (2014) and accordingly Marugán-Cruz et al. (2016) apply the analytical solution to stress components considering radially varying temperature $T = T(r)$ according to Faupel and Fischer (1981) for simple plane strain. As Marugán-Cruz et al. (2016) demonstrates, with $B_1 = D_1 = 0$ this corresponds to the more general solution to $T = T(r,\varphi)$ additionally presented herein (see also above) for comparison purposes. Similar to the results derived from the comparison of 1D and 2D thermal models in Sec. 2.2.1, errors in calculation of thermal stress due to neglection of circumferential temperature gradient increase with decreasing Biot number N_{Bi}. For the error to be less than 5 %, according to Marugán-Cruz et al. (2016), $N_{\mathrm{Bi}} \gtrsim 10$ is required.

In Neises et al. (2014), thermal stress inside an alloy 230 absorber tube with sCO_2 as HTF is approximated by analogy with Flores et al. (2014), assuming generalized plain strain condition. Additionally, for evaluation of creep-fatigue damage, normal stresses due to internal pressure are superimposed as given in Timoshenko and Goodier (1951) (compare Logie et al. (2018); Nithyanandam and Pitchumani (2016) et al.).

Liao et al. (2014) extends the model from Smith (1992) taking into account finite tube wall thickness within the thermal model and performs a parameter and sensitivity study on AFD for the Solar Two receiver. The heat transfer at the inner tube wall (316 stainless steel) is modeled with the Gnielinski correlation taken from Bergmann et al. (2011) and assuming $f = \text{const.} = 0.054$ (Kolb,

---

the tube crown with thermal stress derived applying the simplified analytical model as given in Smith (1992), concluding that the simplified model significantly overpredicts equivalent stress.

[14]As further outlined in Logie et al. (2018), higher harmonics, i.e. terms with $n > 1$, in the generalized plane harmonic Fourier series for $T_\varphi(r,\varphi) = \sum_{n=1}^{\infty} \left(A_n\ r^n + B_n\ r^{-n}\right)\ \cos(n\varphi) + \left(C_n\ r^n + D_n\ r^{-n}\right)\ \sin(n\varphi)$ can be neglected according to Boley and Weiner (1960); Timoshenko and Goodier (1951). Remaining (in Cartesian coordinates) linear terms $A_1\ r\cos(\varphi)$, $C_1\ r\sin(\varphi)$ do not induce thermal stress as long as surface traction, body forces and any displacement singularities are ignored, satisfying Laplacian equation (Boley and Weiner, 1960; Irfan and Chapman, 2009)).

2011).

Rodríguez-Sánchez et al. (2015) simulates the annual operation of an external alloy 800H tubular receiver coupled with the Gemasolar field for different flow pattern configurations. The thermal simulations are based upon previous work (Rodríguez-Sánchez et al., 2014a,b), thermal stress σ_{eq} at the irradiated tube crown is approximated by analogy with Liao et al. (2014), neglecting the contribution of temperature difference in circumferential direction (cf. Rodríguez-Sánchez et al. (2014a))[15].

In a parameter study, Khanna et al. (2015) derives analytical expressions for temperature distribution and deflection from focal line of a parabolic trough absorber tube[16]. Taking into account temperature variation in radial and circumferential direction, i.e. $T = T(r, \varphi)$, 2D Laplacian conduction equation is solved with temperature dependent K using the method of separation of variables. Applying net radiation method with temperature dependent tube emissivity, Neumann boundary condition at the outer boundary of the tube domain, which – besides radiation exchange between glass cover and outer tube – implicitly considers exchange between cover and surroundings and convective losses, is linearized[17]. Differential view factors between tube and glass cover surfaces are derived analytically as function of relative angle $\Delta\varphi$, axially discretizing absorber tube and glass cover into segments of minimum length Δz allowing for neglection of radiation exchange between axially displaced elements (see also Rodríguez-Sánchez et al. (2014b)). $T(r, \varphi)$ is expressed similarly as before (Irfan and Chapman (2009) et al.) as $T = T_r(r) + T_\varphi(r, \varphi) = A_0 + B_0\ \ln(r) + \sum_{n=1}^{\infty} (A_n\ r^n + B_n\ r^{-n})\ \cos(n\varphi) + (C_n\ r^n + D_n\ r^{-n})\ \sin(n\varphi)$,

[15] In Rodríguez-Sánchez et al. (2018), the contribution of thermal stress due to circumferential temperature gradients is approximated in accordance with Liao et al. (2014).

[16] Although in parabolic trough systems operational and boundary conditions (e.g. solar flux distribution, mechanical constraints), materials etc. generally differ from those of tower systems, the analytical approaches in Khanna et al. (2015) seemed worth mentioning here: Besides the approach for the mechanical model in line with more recent work for vertical tubes from Logie et al. (2018) et al., an analytical solution to 2D Laplacian conduction equation including thermal losses at the outer domain boundaries is presented.

[17] Alternatively, an iterative solution to 2D conduction equation is proposed (cf. Logie et al. (2018)).

amounting to derivation of analytical expressions for coefficients A_0, B_0 and A_n, B_n with $C_n = D_n = 0$ (assuming axial symmetry of $T(r, \varphi)$).

Sánchez-González et al. (2017) implements the AFD-concept from Vant-Hull (2002) in an aiming model pursueing to maximize solar flux yield within precomputed flux limits and illustrates its functionality by the example of a Gemasolar-like receiver system model. The thermal simulations are – similar to Rodríguez-Sánchez et al. (2015) – based upon previous work from Rodríguez-Sánchez et al. (2014b,a). Thermal stress σ_{eq} is approximated as in Rodríguez-Sánchez et al. (2015), explicitly considering finite wall thickness (Irfan and Chapman, 2009; Young and Budynas, 2002)[18].

Following the methodology presented in Logie et al. (2018) for mechanical modeling, additionally accounting for pressure difference between inner and outer tube surface, Conroy et al. (2018a,b) derive linear-elastic stress components for creep-fatigue damage analysis based upon thermal modeling as described above (Sec. 2.2.1). For calculation of axial stress, zero axial force with annulled bending moment is postulated.

Laporte-Azcué et al. (2020a) expand the expressions for stress components of 2D thermoelasticity as given in Logie et al. (2018) et al. taking into account temperature dependency of α within the stress terms due to $T_r(r)$. What is more, an analytical expression of total axial stress $\sigma_z = \sigma_z^{\mathrm{b}} + \sigma_z^{\nu}$ superimposing contributions due to bending and axial expansion (σ_z^{b}) and triaxial stress state (σ_z^{ν}) is presented. Herein, besides α, temperature dependence of E is explicitly acknowledged. Using beam theory and hypothesis of free axial expansion, the expression for σ_z^{b} is extended from Noda et al. (2003) to account for influence of reaction forces due to axially distributed beam supports (such as clips).

Montoya et al. (2020) examines the influence of longitudinal clips and mechanical boundary conditions on thermally induced deflection and stress, based upon the thermal model from Rodríguez-Sánchez et al. (2014a) and expres-

[18]Later on, in an extended parameter study following the same methodology (Sánchez-González et al., 2020), the contribution of temperature difference in circumferential direction to thermal stress is acknowledged using an analytical expression as in Liao et al. (2014) instead.

sions for stress components of 2D thermoelasticity as in Logie et al. (2018). Axial stress is calculated similar to Laporte-Azcué et al. (2020a), using one-dimensional beam theory for derivation of σ_z^{b}.

González-Gómez et al. (2021), based upon ASME Boiler and Pressure Vessel Code, Section III, Division 1, Subsection NH (ASME BPVC-III-1 NH) (cf. ASME (2015)), presents a methodology for calculation of creep-fatigue damage including plastic strain and stress relaxation effects (see below, Sec. 3.2). Thermal calculations are performed using the model from Rodríguez-Sánchez et al. (2014a), thermal stress components are derived as proposed in Laporte-Azcué et al. (2020a), assuming generalized plain strain for simplicity. For completeness, pressure induced stress is also accounted for, applying the expressions as specified in Logie et al. (2018) et al.

3. Damage modeling

3.1. Overview

In the context of tubular receiver systems, the influence of operation modes and optimization strategies on reliability and service life of components is typically considered with respect to creep-fatigue damage accumulating over time as dominant failure mechanism.

Besides creep-fatigue, corrosive nature of molten salt at elevated temperatures is commonly taken into account within definition of operating limits. A pragmatic and conservative approach commonly undertaken in literature is the restriction of local film temperatures to an appropriate limit such as 600 °C (Smith, 1992; Vant-Hull, 2002) in order to reduce both corrosion and salt decomposition in the first place (Bradshaw and Goods, 2001).

Fig. 3 illustrates principal steps required for top-down analysis of creep-fatigue damage as widely applied in literature (see below, Sec. 3.2), basically following the methodology from ASME BPVC-III-5 (formerly described in ASME BPVC-III-1 NH and ASME CC N-47):

Looping through time intervals Δt_i[19] of appropriate length – depending on local change rates $\partial/\partial t$ of essential field variables $T(\mathbf{x}, t)$, $\boldsymbol{\sigma}(\mathbf{x}, t)$, $\boldsymbol{\varepsilon}(\mathbf{x}, t)$, local reference temperature $T_{\text{ref}}(\mathbf{x}, \Delta t_i)$, equivalent stress $\sigma_{\text{eq}}(\mathbf{x}, \Delta t_i)$ and strain range $\Delta\varepsilon_{\text{eq}}(\mathbf{x}, \Delta t_i)$ are determined from the underlying thermomechanical model (see above). In case of a linear-elastic mechanical modeling approach, which is commonly applied in face of otherwise drastically increased model complexity (see Sec. 2.2.1 and, herein, in particular Barua et al. (2019); Fork et al. (2012)), respective elastic values are typically modified to account for plastic strain effects[20]. Based upon failure curves derived from lab data, creep-rupture time t_{c} and number of cycles to fatigue failure N_{f} are determined as functions of $\mathbf{x}$ and Δt_i. In order to increase conservativity in light of neglected off-nominal conditions (Sec. 1) and other uncertainties, in addition to nominal, design failure curves are applicable. Supplementarily, σ_{eq}, $\Delta\varepsilon_{\text{eq}}$ can be individually adjusted with global or – to account for notch effects, for instance (Doupis et al., 2016; González-Gómez et al., 2021) – locally differing safety factors SF_{c}, SF_{f}. In the next step, creep and fatigue damage $D_{\text{c}}(\mathbf{x}, t_i)$, $D_{\text{f}}(\mathbf{x}, t_i)$ are calculated from preceding values at time t_{i-1} applying linear damage rule. Herein, as an alternative to SF_{c}, SF_{f}, safety factors SF_{c}^*, SF_{f}^* can be directly imposed on damage increments. Eventually, for $i = n$, accumulated damage $D_{\text{c}}(\mathbf{x}, t_n)$, $D_{\text{f}}(\mathbf{x}, t_n)$ is evaluated. If a parameter study is performed in order to determine design parameters such as AFD, the process described is iterated until service life/local creep-fatigue interaction limit at any location $\mathbf{x}$ is achieved for $t = t_n$. As before, both interaction model data and input variables D_{c}, D_{f} can be manipulated applying safety factors $\text{SF}_{\text{c}}^{**}$, $\text{SF}_{\text{f}}^{**}$ or SF_{total}.

[19]Though, in Fig. 3, accumulation of local damage at time t_n is broken down to a summation over arbitrary time intervals Δt_i in favor of generality. In practice, extrapolation of boundary conditions for operation – especially local solar irradiation – amounts to definition of characteristic (design) load cycles, their particular duration and frequency of occurence within desired service life $t_n - t_0$. This characterization of load cycles ranges from restriction to a sequence of 'binary' design cycles (e.g. Neises et al. (2014); Rao et al. (2021)) over grouped forecast insolation cycles (Conroy et al., 2018a,b; Kistler, 1987) up to consideration of short-term transients due to cloud passage etc. (Flesch et al., 2017; Fork et al., 2012).

[20]Regarding general limits for application of elastic analysis with respect to stress and strain, the reader is referred to ASME BPVC-III-5 Appendix HBB-T-1430.

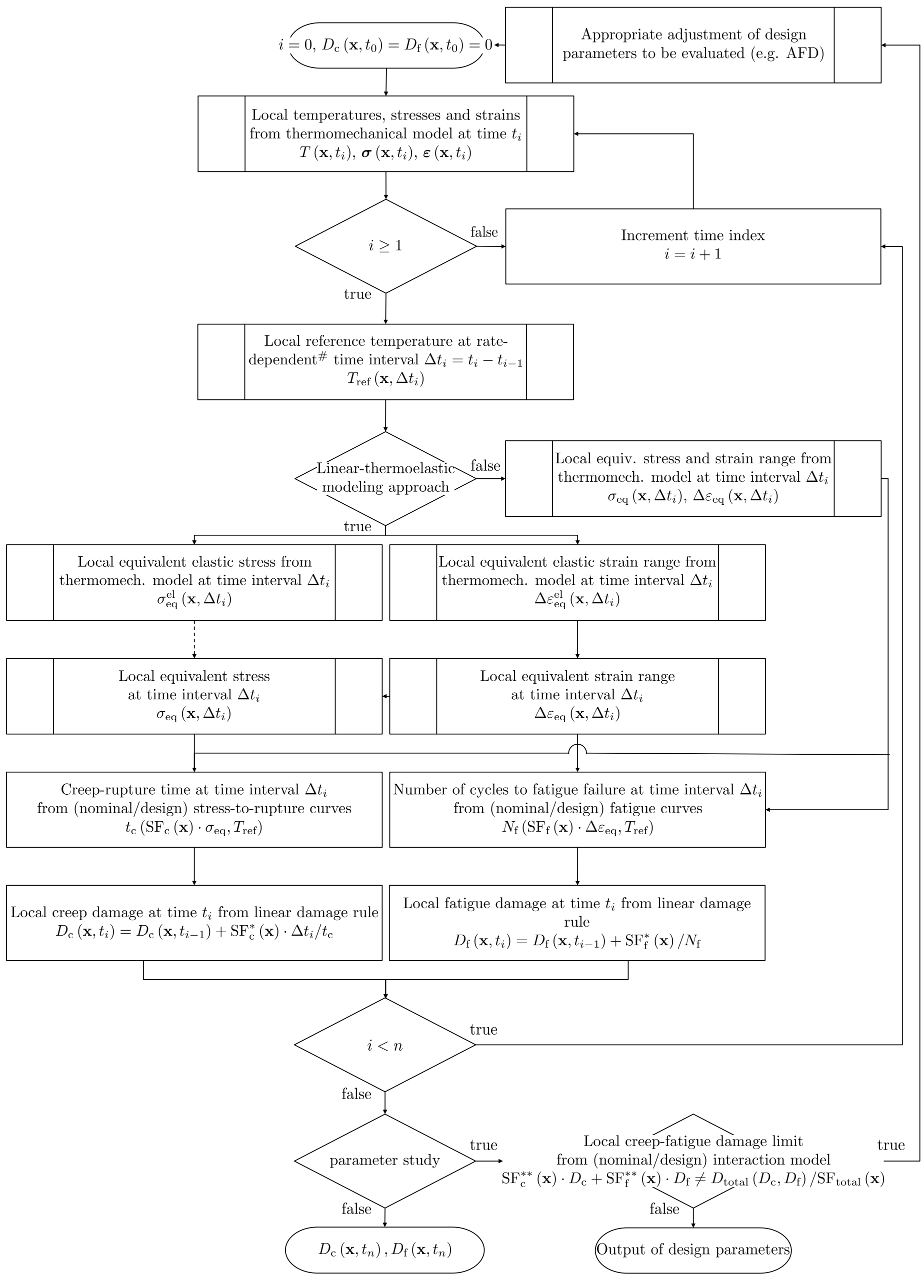

Time interval Δt_i depends on extrapolated design load, corresponding local temperature, stress and strain rates

Figure 3: Principal analysis steps for top-down creep-fatigue damage modeling approaches in literature based upon field variables $T(\mathbf{x}, t)$, $\boldsymbol{\sigma}(\mathbf{x}, t)$, $\boldsymbol{\varepsilon}(\mathbf{x}, t)$, following ASME BPVC-III-5

3.2. Damage modeling methods applied in literature

In this section, essential characteristics of damage modeling methods applied in literature are presented in detail. An overview of (creep-fatigue) damage modeling methods is given in Appendix A, Tab. A.5.

Narayanan et al. (1985) evaluates creep-fatigue damage for components of a molten salt tubular receiver at elevated temperatures applying linear damage rule as in ASME (1980), CC N-47 (compare Smith (1992)), introducing modifications to reduce the level of conservativity inherent in CC N-47 based upon Berman et al. (1979). First, as already briefly addressed above, usage of inelastic fatigue curves is proposed, multiplying the strain ranges $\Delta\varepsilon_{\mathrm{eq}}^{\mathrm{el}}$ obtained from a linear-elastic mechanical analysis with a correction factor of 1.1. Second, creep-rupture damage is evaluated depending on the magnitude of calculated equivalent stress $\sigma_{\mathrm{eq}}^{\mathrm{el}}$: For $\sigma_{\mathrm{eq}}^{\mathrm{el}} > S_{\mathrm{y}}^{\mathrm{h}} + S_{\mathrm{y}}^{\mathrm{c}}$, i.e. equivalent elastic stress is greater than sum of yield stress at hot and cold leg of cycle – assuming primary membrane/bending plus secondary stresses to be below twice yield stress $S_{\mathrm{y}}^{\mathrm{h}} + S_{\mathrm{y}}^{\mathrm{c}}$ – corresponding creep-rupture time is determined with $S_{\mathrm{y}}^{\mathrm{h}}$ to account for plastic yielding, assuming elastic shakedown regime (compare González-Gómez et al. (2021)). If $S_{\mathrm{y}}^{\mathrm{h}} < \sigma_{\mathrm{eq}}^{\mathrm{el}} \leq S_{\mathrm{y}}^{\mathrm{h}} + S_{\mathrm{y}}^{\mathrm{c}}$, $\max\left(\sigma_{\mathrm{eq}}^{\mathrm{el}} - S_{\mathrm{y}}^{\mathrm{c}}, 0.8\ S_{\mathrm{y}}^{\mathrm{h}}\right)$ is used instead, incorporating residual stresses as found previously (Berman and Rao, 1983) in a conservative manner. Eventually, for $\sigma_{\mathrm{eq}}^{\mathrm{el}} \leq S_{\mathrm{y}}^{\mathrm{h}}$, creep-rupture time is evaluated based upon $\min\left(\sigma_{\mathrm{eq}}^{\mathrm{el}}, 0.8\ S_{\mathrm{y}}^{\mathrm{h}}\right)$. For damage evaluation, $11,000$ diurnal and $19,000$ cloudy cycles of the same severity during 30 years corresponding to 10^5 hours of operation are assumed.

As already mentioned in Sec. 2.2.1, Fork et al. (2012) includes both plastic strain effects and secondary (equilibrium) creep in a 2D mechanical model for creep-fatigue damage analysis. Therefore, two different methods for estimation of service life consumption and accumulated damage are proposed: The first method is based upon ASME BPVC-III-1 NH for a nonlinear mechanical modeling approach, taking into account interaction of creep and fatigue damage for alloy 617. Equivalent strain ranges $\Delta\varepsilon_{\mathrm{eq}}$ are calculated according to ASME

BPVC-III-1 NH, T-1414 with elastic and inelastic strain proportions. Number of cycles to fatigue failure N_f are determined using a combined Basquin and Coffin-Manson expression with both a nominal and a more conservative, design parametrization. Creep-rupture time t_c is determined with a correlation of Mendelson-Roberts-Manson (MRM) type using minimum values for 0.95-percentile and equivalent von Mises stress σ_eq multiplied with safety factors $\mathrm{SF_c} \in \{1.0, 1.5\}$. In the second method, fatigue and creep damage accumulation due to diurnal cycles and cloud transients is directly calculated with experimental creep-fatigue interaction data based upon inelastic strain proportions, introducing an overall safety factor $\mathrm{SF_{total}} = 10$.

For AFD evaluation in Neises et al. (2014), based upon the interim standard of Berman et al. (1979), 10^4 fatigue cycles and 10^5 operating hours under creep load at design conditions are set for simplicity (cf. Conroy et al. (2019a,b); Rao et al. (2021)). Inelastic strain ranges are obtained as in Narayanan et al. (1985), equivalent – von Mises – strain is multiplied with a safety factor $\mathrm{SF_f} = 2.0$. In addition, a lower limit for fatigue damage D_f of 10 % is set[21]. Maximum principle stress σ_1^el together with a safety factor $\mathrm{SF_c} = 1.5$ is used for consideration of creep damage.

In Liao et al. (2014), the maximum admissible strain range $\Delta\varepsilon_\mathrm{adm,f}$ is taken from ASME BPVC-III-1 NH under the assumption of $36,000$ thermal cycles during a 30-year life time as reported in Zavoico (2001).

Rodríguez-Sánchez et al. (2015) introduces – besides minimum flow rate – a maximum film temperature of 650 °C and a maximum admissible thermal stress σ_adm in the amount of one third of the ultimate tensile strength (UTS) according to ASME BPVC-III-1 NH as operational limits.

Doupis et al. (2016) follows the methodology outlined in DIN EN 12952-3/4 (DIN, 2011a,b) for a creep and fatigue damage analysis of the header model

[21] Consequently, in Rao et al. (2021), fatigue damage values of less than 10 % are ignored. In Ortega et al. (2016a), alternatively, fatigue damage is generally fixed at 10 %. With $D_\mathrm{total}\left(D_\mathrm{c}, D_\mathrm{f}\right) = \mathrm{const.} = 1$ as in Neises et al. (2014), creep damage determined with a quadratic Larson-Miller expression is thus limited to 0.9.

examined (see above, Sec. 2.2.1). Therefore, maximum peak stress range is evaluated both globally and in the area of welds applying stress enhancement (notch) factors.

Nithyanandam and Pitchumani (2016) analyzes numbers of cycles to fatigue failure N_f and creep-rupture times t_c for various operating points and designs of $\mathrm{sCO_2}$ tubular receiver systems. N_f is derived from Basquin/Coffin-Manson-type expression with equivalent – linear-elastic von Mises – strain $\varepsilon_\mathrm{eq}^\mathrm{el}$ multiplied by $\mathrm{SF_f} = 2.0$, t_c is determined with MRM-type correlation for alloy 230 based upon average creep data.

In Sánchez-González et al. (2017), film temperatures are limited to 630 °C for alloy 800H to contain corrosion[22]. Maximum admissible thermal stress σ_adm is defined in accordance with Rodríguez-Sánchez et al. (2015).

Conroy et al. (2018a,b) rely on ASME BPVC-III-1 NH for damage accumulation with linear damage rule and material dependent creep-fatigue interaction curves. Similar to Smith (1992), DNI data extrapolated to 30 years of operation is used for grouping of creep load and unique fatigue cycles. Equivalent strain ranges $\Delta\varepsilon_\mathrm{eq}$ are established from von Mises thermal strain modified by correction factors accounting for plastic strain and creep effects. Equivalent stress σ_eq is defined as von Mises load controlled stress, i.e. pressure induced membrane/bending and thermally induced membrane stress.

Similarly, for evaluation of creep-fatigue damage from design by elastic analysis in Barua et al. (2019), strain ranges from the linear-elastic mechanical model are modified according to ASME BPVC-III-5 to account for plastic strain and creep effects. Numbers of cycles to fatigue failure N_f are determined with three different – nominal, CSP and nuclear – fatigue design curves, the latter (CSP, nuclear) implying safety factors of $\mathrm{SF_f} \in \{1.5, 2.0\}$ on strain range or $\mathrm{SF_f^*} \in \{10, 20\}$ on N_f, whichever is more conservative. Stress relaxation curves are derived from isochronous stress-strain curves at respective modified strain

[22] See also Sánchez-González et al. (2020) for derivation of film temperature limits for further alloys based upon admissible metal loss rates.

ranges $\Delta\varepsilon_{\mathrm{eq}}$, resulting creep-rupture times t_{c} are determined both from design and nominal stress-to-rupture curves based upon a Larson-Miller correlation for 0.95-percentile. For design by inelastic analysis[23] (compare Fork et al. (2012); Frantz et al. (2020)), representative strain ranges $\Delta\varepsilon_{\mathrm{eq}}$ and stress relaxation profiles are extracted from the inelastic mechanical model (see above, Sec. 2.2.1). Analog to the elastic analysis, nominal, CSP and nuclear fatigue design curves are taken for determination of N_{f}. Creep-rupture times t_{c} are determined from nominal stress-to-rupture curves, calculating equivalent stress σ_{eq} with Huddleston model and applying three different safety factors $\mathrm{SF_c} \in \{1.0, 1.1, 1.5\}$. Creep-fatigue interaction is generally adopted from alloy 617 for want of more specific data.

Based upon their findings in Conroy et al. (2018c) and Conroy et al. (2018a,b) for thermal and mechanical modeling, in Conroy et al. (2019a,b) a corresponding 2D model of an arbitrary tube section is employed for AFD calculation superimposing thermal and pressure induced stresses and calculating equivalent von Mises stress $\sigma_{\mathrm{eq}}^{\mathrm{el}}$ and strain $\varepsilon_{\mathrm{eq}}^{\mathrm{el}}$. Besides consideration of design stress limits according to ASME BPVC-III-1 NH and maximum material/film temperatures (cf. Rodríguez-Sánchez et al. (2015); Sánchez-González et al. (2017, 2020)), within the creep-fatigue regime, at least 10^4 fatigue cycles and minimum 10^5 operating hours under creep load are stipulated for the various materials investigated (compare Neises et al. (2014); Rao et al. (2021)).

González-Gómez et al. (2021) presents a methodology for calculation of creep-fatigue damage, in principle following ASME BPVC-III-1 NH, however, proposing alternative analytical methods for consideration of plastic strain and stress relaxation effects. Equivalent (von Mises) elastic strain ranges $\Delta\varepsilon_{\mathrm{eq}}^{\mathrm{el}}$ are manipulated depending on corresponding elastic thermal stress $\sigma_{\mathrm{eq,T}}^{\mathrm{el}}$: If $\sigma_{\mathrm{eq,T}}^{\mathrm{el}} < 2S_{\mathrm{y}}$ (elastic or elastic shakedown regime), equivalent strain ranges $\Delta\varepsilon_{\mathrm{eq}}$

[23] Regarding further design methods not elaborated on here for either covering failure modes out of scope of this paper (primary load failure, ratcheting) or considered less significant (creep-fatigue design by elastic perfectly-plastic analysis), the reader is referred to Barua et al. (2019).

are set equal to $\Delta\varepsilon_{\mathrm{eq}}^{\mathrm{el}}$. Otherwise, assuming reverse plasticity regime, $\Delta\varepsilon_{\mathrm{eq}}$ is obtained with a two-fold approach: First, equivalent inelastic stress range $\Delta\sigma_{\mathrm{eq}}$ is obtained from elastic quantities using Neuber's or Glinka-Molski approximation (Glinka, 1985; Moftakhar et al., 1994)[24] together with cyclic stress-strain curve (Glinka, 1985) parametrized for stabilized hysteresis loop data. Second, inelastic strain ranges $\Delta\varepsilon_{\mathrm{eq}}$ are calculated from $\Delta\sigma_{\mathrm{eq}}$ according to Kalnins (2005) and, herein, an approximation of equivalent plastic strain range from Mao et al. (2016); Moftakhar et al. (1994). N_{f} is determined from $\Delta\varepsilon_{\mathrm{eq}}$ with an implicit Coffin-Manson expression. Similarly to the approach for derivation of $\Delta\varepsilon_{\mathrm{eq}}$, equivalent stress σ_{eq} is set equal to $\sigma_{\mathrm{eq}}^{\mathrm{el}}$ for $\sigma_{\mathrm{eq}}^{\mathrm{el}} \leq S_{\mathrm{y}}$. In elastic shakedown regime ($S_{\mathrm{y}} < \sigma_{\mathrm{eq}}^{\mathrm{el}}$ and $\sigma_{\mathrm{eq,T}}^{\mathrm{el}} < 2S_{\mathrm{y}}$) σ_{eq} is calculated from elastic quantities using Neuber's or Glinka-Molski approximation and monotonic stress-strain curve as in Glinka (1985). For $\sigma_{\mathrm{eq,T}}^{\mathrm{el}} \geq 2S_{\mathrm{y}}$, the cyclic stress-strain curve is applied instead. Stress relaxation $\sigma_{\mathrm{eq}}^{\mathrm{relax}}$ is accounted for with an analytical expression derived from a Norton-Bailey creep strain rate model assuming constant total strain and uniaxial stress state. Eventually, introducing a safety factor $\mathrm{SF_c} = 1.1$ (cf. Barua et al. (2019)), creep-rupture times t_{c} can be determined with $\mathrm{SF_c} \cdot \sigma_{\mathrm{eq,eff}} = \mathrm{SF_c} \cdot \max\left(\sigma_{\mathrm{eq}} - \sigma_{\mathrm{eq}}^{\mathrm{relax}}, \sigma_{\mathrm{eq,p}}\right)$ from MRM-type stress-to-rupture curves.

4. Conclusion and outlook: Real-time monitoring of service life consumption

Contemporary thermomechanical and damage modeling methods presented in Sec. 2.2 and Sec. 3.2 provide a variety of approaches in order to exploit the improvement potential in operational optimization of tubular receiver systems regarding consideration of service life consumption based upon the traditional AFD-concept from Smith (1992); Vant-Hull (2002).

[24] As González-Gómez et al. (2021) states these methods – developed as approximate techniques to estimate the redistribution of stress caused by plastic flow in a zone of stress concentration – are valid when the plastic area is relatively small and surrounded by enough elastic zone.

First of all, the methods presented in Sec. 2.2.2 for analytical calculation of local temperature T as well as stress $\boldsymbol{\sigma}$ and strain $\boldsymbol{\varepsilon}$ enable much more detailed modeling of local load states and boundary conditions compared to Smith (1992).

The 1D thermal modeling approach given in Smith (1992) can be extended beginning with consideration of finite wall thickness and a modified approach for $\dot{q}^{\mathrm{i,C}}$ (Liao et al., 2014, et al.), up to implementation of an analytical methodology for solution to 2D Laplacian conduction equation additionally accounting for local radiative heat exchange $\dot{q}^{\mathrm{o,R}}$ and convective losses $\dot{q}^{\mathrm{o,C}}$ at outer domain boundaries (Khanna et al., 2015). Then, regarding analytical modeling of stress and strain, Irfan and Chapman (2009); Yang and Lee (1971) suggest a series solution to thermally induced normal and shear stress components allowing for radially and axially varying temperature distribution $T = T(r, z)$. Instead, for stress components resulting from radially and circumferentially varying temperature distribution $T = T(r, \varphi)$, the analytical solution approach from Conroy et al. (2018a,b); Logie et al. (2018) et al. is applicable, superimposing contributions due to pressure (difference) at domain boundaries. Recently, pursuant to Laporte-Azcué et al. (2020a); Montoya et al. (2020) this approach can be extended once more presenting an analytical expression of total axial stress σ_z, acknowledging temperature dependence of E and α.

Second, for modeling of local damage in extension of Smith (1992), both creep damage D_{c} and – depending on availability of material specific data – creep-fatigue damage interaction can be taken into account based upon ASME BPVC-III-5 widely applied in literature, though typically modified in favor of applicability, reduced level of conservativity or for want of appropriate data. What is more, fatigue damage D_{f} can be approximated more accurately as well, considering plastic strain effects[25].

[25]Nevertheless, at this point it should be noted that an accurate – i.e. absolute – prediction of service life is still an highly ambitious undertaking both regarding accurate modeling of material behaviour, corresponding levels of local stress as well as strain (cf. e.g. Fork et al.

In case of linear-elastic modeling approach which is commonly preferred due to considerably increased complexity of and massive computational resources required for inelastic models, equivalent stress $\sigma_{\mathrm{eq}}^{\mathrm{el}}$ and strain range $\Delta\varepsilon_{\mathrm{eq}}^{\mathrm{el}}$ are typically defined as von-Mises stress and strain. Following Neises et al. (2014), modification of equivalent elastic strain range $\Delta\varepsilon_{\mathrm{eq}}^{\mathrm{el}}$ and derivation of stress σ_{eq} from isochronous stress-strain curves with $\Delta\varepsilon_{\mathrm{eq}}$ as in ASME BPVC-III-5 can be simplified with a correction factor of 1.1 from Narayanan et al. (1985) for $\Delta\varepsilon_{\mathrm{eq}}^{\mathrm{el}}$ and maximum principle stress σ_1^{el} for σ_{eq}. Alternatively, a more elaborate modification of $\Delta\varepsilon_{\mathrm{eq}}^{\mathrm{el}}$ depending on equivalent elastic thermal stress regime is proposed in González-Gómez et al. (2021); equivalent stress σ_{eq} is similarly derived from elastic stress quantities, accounting for stress relaxation. For determination of creep-rupture time t_{c} and number of cycles to fatigue failure N_{f}, depending on desired conservativity and/or availability of appropriate lab data, both nominal and (CSP, nuclear) design curves are applicable with safety factors SF between 1.0 and 2.0.

Regarding impact of corrosive nature of molten salt on local damage accumulation, its containment via restriction of local film temperatures, as already proposed in Smith (1992), still seems to be the most common and pragmatic approach. In order to reduce inherent conservativeness, however, e.g. Rodríguez-Sánchez et al. (2015); Sánchez-González et al. (2017) propose 650 °C, 630 °C, respectively, as film temperature limit for alloy 800H (compare Bradshaw and Goods (2001)) in contrast to the commonly stipulated 600 °C.

In principle, in place of an analytical calculation of local temperature, stress and strain, 'heuristic' numerical models as described in Sec. 2.2.1 are applicable for that purpose, allowing e.g. for more elaborate consideration of actual receiver

(2012)) and local damage accumulation. The latter is typically modeled extrinsically applying parametrized failure curve models based upon lab data (see also Tab. A.5 in Appendix A) generated under idealized conditions and is thus applicable to a specific solar receiver system and its transient, multiaxial load states only with some reservations. Moreover, the application of safety factors introduced for this reason results in a considerable variation in calculated damage accumulation, depending on stipulated level of conservativity (Barua et al., 2019; Fork et al., 2012).

geometry, local boundary conditions and constitutive modeling.

The suitability of heuristic numerical models within the bottom-up approach plead for in Sec. 1, however, – ultimately amounting to real-time, condition-based operational and maintenance strategy optimization – is basically restricted by respective model complexity and available computational resources[26]. Thus, solely relying on conventional modeling and reduction methods, a trade-off between accuracy of thermomechanical modeling on the one hand and temporal resolution on the other hand is inevitable.

As consequence, one objective to be demonstrated in upcoming functional testing of a bottom-up approach for local damage accumulation and monitoring of service life consumption at a pilot scale test facility (cf. Frantz et al. (2020)) comprises the resolution of said opposition between modeling accuracy and temporal resolution via acceleration techniques based upon efficient model parametrization and artificial intelligence (AI).

After all, besides the benefits already outlined in Sec. 1, real-time monitoring of local load states and service life consumption is expected to notably reduce need for safety margins as far as consideration of off-nominal conditions is concerned, consequently increasing economic viability of molten salt tubular receiver systems.

5. Declaration of competing interest

The authors declare that they have no known competing financial interests or personal relationships that could have appeared to influence the work reported in this paper.

[26]Insofar, this does in particular apply for models going even beyond the aforementioned, heuristic approaches, i.e. 3D-CHT and 3D mechanical models from Sec. 2.2.1 (compare Barua et al. (2019); Frantz et al. (2020); Fritsch et al. (2017); Yang et al. (2012)). In order to ensure that in that sense inevitable modeling errors are individually acceptable, as already suggested in footnote 12, a (partial/representative) validation of calculated load states and corresponding, local field variables analyzed with a detailed 3D modeling approach or an experimental setup appropriately accounting for receiver geometry, local boundary conditions and material behavior seems indispensable.

6. Acknowledgements

The projects within which this work was carried out are funded by the German Federal Ministry for Economic Affairs and Energy under the funding codes 03EE5006 and 0324327. The responsibility for the content of this publication lies with the authors.

Appendix A. Overview and essential characteristics of thermomechanical and damage modeling methods

Table A.1: Overview and essential characteristics of numerical approaches for thermal modeling methods in literature (cf. Sec. 2.2.1)

model	**domain**	**field equations**	**constitutive laws**			**properties**	**calculation of thermal losses**		**references**
			turbulence model	friction factor f	Nusselt number $N_{\mathrm{Nu}}^{\mathrm{i}}$		convective	radiative	
3D vertical tube	fluid	3D steady-state, RANS, Boussinesq approximation	k-ω-SST	–	–	$f(T)$	–	–	(Fritsch et al., 2017)
		3D steady-state, incompressible RANS	k-ε	–	–	const.	–	–	(Chang et al., 2014)
		1D (z) steady-state (enthalpy flow)	–	(Petukhov, 1970)	(Gnielinski, 1976), cf. Bergmann et al. (2011)	$f(T)$	–	–	(Conroy et al., 2018c; Xu et al., 2018)

3D vertical tube(s)	fluid	3D steady-state, RANS	k-ε	–	–	$(\overline{\overline{\rho}}, \overline{\overline{\mu}} =)$ $f(T)$	–	–	(Du et al., 2016; Flesch et al., 2017; Rodríguez-Sánchez et al., 2014b; Qiu et al., 2019; Yang et al., 2012; Ying et al., 2020)
		1D (z) steady-state enthalpy flow	–	(Verein Deutscher Ingenieure, VDI-Gesellschaft Verfahrenstechnik und Chemieingenieurwesen, 2010)	(Verein Deutscher Ingenieure, VDI-Gesellschaft Verfahrenstechnik und Chemieingenieurwesen, 2010)	$f(T)$	–	–	(Fritsch et al., 2017), cf. Frantz et al. (2017, 2020); Uhlig et al. (2018)
		–, predefined, linearly increasing bulk temperature	–	–	n.a.	$f(T)$	–	–	(Barua et al., 2019)
representative, 3D vertical tube half-shells	fluid	1D (z) steady-state enthalpy flow	–	–	n.a.	$f(T)$	–	–	(Montoya et al., 2018; Rodríguez-Sánchez et al., 2014b, 2015; Sánchez-González et al., 2017)
3D vertical tubes	fluid	1D (z) (two-phase) flow	–	n.a.	n.a.	n.a.	–	–	(Flesch et al., 2017)

		1D (z) steady-state (enthalpy flow)	–	Colebrook (1939)	(Gnielinski, 1976)	$f(T)$	–	–	(Zhang et al., 2015)
			–	(Petukhov, 1970)	(Gärtner et al., 1974)	$f(T)$	–	–	(Conroy et al., 2018a,b)
			–	–	(Gnielinski, 2013)	$f(T)$	–	–	(Laporte-Azcué et al., 2020a; Rodríguez-Sánchez et al., 2018)
3D outlet header	fluid	–, precalculated bulk temperature and pressure	–	–	Dittus-Boelter, segmentally averaged enhanced turbulence factors	n.a.	–	–	(Doupis et al., 2016)
3D header and connection tubes	fluid	–, precalculated bulk temperature	–	–	CFD-based	n.a.	–	–	(Uhlig et al., 2018), cf. Frantz et al. (2020)
3D coiled tube receiver	fluid	1D steady-state enthalpy flow	–	explicit expression	(Gnielinski, 1976), spiral correction factor	n.a.	–	–	(Rao et al., 2021)
2D (r, z) vertical tube segment	fluid	2D (r, z) steady-state, RANS	k-ε	–	–	$f(T)$	–	–	(Nithyanandam and Pitchumani, 2016)

2D (r, φ) horizontal tube segment	fluid	2D (r, φ) steady-state, incompressible RANS, fully developed flow	(Cess, 1958)	–	–	const.	–	–	(Flores et al., 2014; Marugán-Cruz et al., 2016)
		1D (z) steady-state	–	(Petukhov, 1970)	(Gnielinski, 1976)	const.	–	–	(Marugán-Cruz et al., 2016)
2D (r, φ) horizontal tube half-shell segment	fluid	1D (z) steady-state enthalpy flow	–	–	Dittus-Boelter	$f(T)$	–	–	(Logie et al., 2018)
3D vertical tube	solid	3D transient	–	–	–	$K = f(T)$	natural and forced (Siebers and Kraabel, 1984)	net radiation method	(Xu et al., 2018)
		3D steady-state	–	–	–	const.	–	–	(Chang et al., 2014; Qiu et al., 2019; Yang et al., 2012; Ying et al., 2020)
			–	–	–	$f(T)$	n.a.	n.a.	(Flesch et al., 2017)
			–	–	–	$f(T)$	–	–	(Du et al., 2016)

3D vertical tube(s)	solid	3D transient	–	–	–	const.	n.a./CFD-based	n.a.	(Fritsch et al., 2017), cf. Frantz et al. (2017, 2020); Uhlig et al. (2018)
		3D steady-state	–	–	–	$f(T)$	n.a.	n.a.	(Barua et al., 2019)
			–	–	–	$K = f(T)$	implicit, air included in computational domain	Discrete Ordinate model	(Rodríguez-Sánchez et al., 2014b)
		1D (r) steady-state	–	–	–	n.a.	natural and forced (Siebers and Kraabel, 1984)	net radiation method, 2D view factors with Crossed-Strings method	(Conroy et al., 2018a,b,c)
representative, 3D vertical tube half-shells	solid	1D (r) steady-state	–	–	–	$f(T)$	natural and forced (Siebers and Kraabel, 1984)	net radiation method, 2D view factors with Crossed-Strings method	(Montoya et al., 2018)
		1D (r) steady-state, homogeneous heat flux	–	–	–	$K = f(T)$	natural and forced (Siebers and Kraabel, 1984)	net radiation method, 2D view factors with Crossed-Strings method	(Rodríguez-Sánchez et al., 2014b)

		1D (r) steady-state, homogeneous temperature	–	–	–	$K = f(T)$	natural and forced (Siebers and Kraabel, 1984)	net radiation method, 2D view factors with Crossed-Strings method	(Rodríguez-Sánchez et al., 2014b, 2015)
3D vertical tubes	solid	1D (r) steady-state	–	–	–	$f(T)$	natural and forced (Siebers and Kraabel, 1984; Li et al., 2010)	net radiation method, view factors with Monte-Carlo method	(Zhang et al., 2015)
		1D (r) steady-state, homogeneous temperature	–	–	–	$f(T)$	natural and forced (Siebers and Kraabel, 1984)	net radiation method, 2D view factors with Crossed-Strings method	(Laporte-Azcué et al., 2020a; Rodríguez-Sánchez et al., 2018)
		n.a./transient	–	–	–	n.a.	n.a.	n.a.	(Flesch et al., 2017)
3D outlet header	solid	3D transient	–	–	–	n.a.	–	–	(Doupis et al., 2016)
3D header and connection tubes	solid	3D transient	–	–	–	n.a.	–	–	(Uhlig et al., 2018), cf. Frantz et al. (2020)
3D coiled tube receiver	solid	3D steady-state	–	–	–	const.	n.a.	Monte-Carlo ray tracing method	(Rao et al., 2021)

(quasi-)1D, projected tubes	solid	(quasi-)1D steady-state	–	–	–	const.	n.a.	n.a.	(Fritsch et al., 2017)
2D (r, z) vertical tube segment	solid	2D (r, z) steady-state	–	–	–	$f(T)$	10 W/m^2 K from (Ho and Iverson, 2014)	net radiation method	(Nithyanandam and Pitchumani, 2016)
2D (r, φ) horizontal tube segment	solid	2D (r, φ) steady-state	–	–	–	const.	–	–	(Flores et al., 2014; Marugán-Cruz et al., 2016)
2D (r, φ) horizontal tube half-shell segment	solid	2D (r, φ) steady-state	–	–	–	const.	30 W/m^2 K from (Siebers and Kraabel, 1984)	net radiation method	(Logie et al., 2018)

Table A.2: Overview and essential characteristics of numerical approaches for mechanical modeling methods in literature (cf. Sec. 2.2.1)

model	**domain**	**field equations**	**constitutive laws**	**properties**	**mechanical loads**			**references**
			stress tensor $\boldsymbol{\sigma}$		T	p	$\mathbf{g}$	
3D vertical tube(s)	solid	n.a.	inelastic, J_2-plasticity with Voce hardening model, creep rate based on power law approach	$f(T)$	•	n.a.	n.a.	(Barua et al., 2019)

		n.a.	linear-thermoelastic	$f(T)$	•	n.a.	n.a.	(Barua et al., 2019)
representative 3D vertical tube	solid	3D quasi-static	linear-thermoelastic	n.a.	•	•	–	(Ortega et al., 2016a)
3D tube including curved in-/outlet regions	solid	3D quasi-static[27]	linear-thermoelastic	$f(T)$	•	–	–	(Montoya et al., 2018)
3D outlet header	solid	n.a.	n.a.	n.a.	•	•	–	(Doupis et al., 2016)
3D panel including header and connection tubes	solid	3D quasi-static	linear-thermoelastic	n.a.	•	•	•	(Uhlig et al., 2018)
3D billboard-shaped receiver	solid	n.a.	inelastic, Chaboche model, creep rate based on Norton-Bailey power law[28]	n.a.	•	•	n.a.	(Frantz et al., 2020)
3D coiled tube receiver	solid	3D quasi-static	linear-thermoelastic	const.	•	•	n.a.	(Rao et al., 2021)
2D (r, z) vertical tube segment	solid	n.a.	inelastic, creep rate based on Norton power law and Arrhenius rate	$f(T)$	•	•	n.a.	(Fork et al., 2012)

[27] At section with maximum temperature, 2D (φ, z) quasi-static (shell elements) elsewhere.
[28] For absorber tube sections, elastic-perfectly plastic approach elsewhere.

Table A.3: Overview and essential characteristics of analytical approaches for thermal modeling methods in literature (cf. Sec. 2.2.2)

model	**domain**	**field equations**	**constitutive laws**			**properties**	**calculation of thermal losses**		**references**
			turbulence model	friction factor f	Nusselt number $N_{\mathrm{Nu}}^{\mathrm{i}}$		convective	radiative	
3D vertical tube(s)	fluid	1D (z) steady-state enthalpy flow	–	0.054 from (Kolb, 2011)	(Bergmann et al., 2011)	$f(T)$	–	–	(Liao et al., 2014), cf. (Kistler, 1987; Smith, 1992; Vant-Hull, 2002)
3D horizontal tube(s)	fluid	1D (z) steady-state enthalpy flow	–	n.a.	n.a.	n.a.	–	–	(Khanna et al., 2015)
3D vertical tube(s)	solid	1D (r) steady-state	–	–	–	$f(T)$	–	–	(Liao et al., 2014), cf. (Kistler, 1987; Smith, 1992; Vant-Hull, 2002)
3D horizontal tube(s)	solid	2D (r, φ) steady-state	–	–	–	$K = f(T)$	n.a.	net radiation method, 2D (differential) view factors	(Khanna et al., 2015)

Table A.4: Overview and essential characteristics of analytical approaches for mechanical modeling methods in literature (cf. Sec. 2.2.2)

model	**domain**	**field equations**	**constitutive laws**	**properties**	**mechanical loads**			**references**
			stress tensor $\boldsymbol{\sigma}$		T	p	$\mathbf{g}$	
3D (vertical) tube	solid	3D quasi-static, $T = T(r, z)$	linear-thermoelastic	const.	•	–	–	(Irfan and Chapman, 2009; Yang and Lee, 1971)
		3D quasi-static, $T = T(z)$	linear-thermoelastic	const.	•	–	–	(Irfan and Chapman, 2009; Lee, 1966)
		2D (r, φ) quasi-static, $T = T(r, \varphi)$ (separate solution to axial stress σ_z)	linear-thermoelastic	$\alpha = f(T)$ within stress terms due to $T_r(r)$, $E, \alpha = f(T)$ within calculation of axial stress term σ_z^{b}	•	(•)	–	(González-Gómez et al., 2021; Laporte-Azcué et al., 2020a)

2D (r, φ) quasi-static, $T = T(r, \varphi)$ (separate solution to axial stress σ_z)	linear-thermoelastic	const.	•	(•)	–	(Conroy et al., 2018a,b; Irfan and Chapman, 2009; Khanna et al., 2015; Logie et al., 2018; Marugán-Cruz et al., 2016; Montoya et al., 2018, 2020), cf. (Boley and Weiner, 1960; Goodier, 1957; Timoshenko and Goodier, 1951)
2D (r, φ) quasi-static, $T = T(r)$ (separate solution to axial stress σ_z)	linear-thermoelastic	const.	•	(•)	–	(Flores et al., 2014; Liao et al., 2014; Marugán-Cruz et al., 2016; Neises et al., 2014; Nithyanandam and Pitchumani, 2016; Rodríguez-Sánchez et al., 2014a, 2015, 2018; Sánchez-González et al., 2017, 2020)[29], cf. (Faupel and Fischer, 1981; Timoshenko and Goodier, 1951)

[29] In Liao et al. (2014); Rodríguez-Sánchez et al. (2014a, 2015, 2018); Sánchez-González et al. (2017, 2020), the analysis is restricted to the tube crown, in Liao et al. (2014); Rodríguez-Sánchez et al. (2014a, 2015, 2018); Sánchez-González et al. (2020) in conjunction with the assumption of a thin-walled tube.

Moreover, in Liao et al. (2014); Rodríguez-Sánchez et al. (2018); Sánchez-González et al. (2020), an approximate expression for consideration of thermal strain/stress due to average circumferential – front-to-back – temperature difference from Young and Budynas (2002) is added.

Table A.5: Overview and essential characteristics of top-down creep-fatigue damage modeling methods in literature following ASME BPVC-III-5 (cf. Sec. 3.1-3.2 and, herein, Fig. 3)

tensor transformation		**modification of elastic values**		**failure curve model**		**safety factors**	**interaction model**	**references**
$\boldsymbol{\sigma}$	$\boldsymbol{\varepsilon}$	$\sigma_{\mathrm{eq}}^{\mathrm{el}}$	$\Delta\varepsilon_{\mathrm{eq}}^{\mathrm{el}}$	stress-to-rupture	fatigue			
n.a.	n.a.	$\sigma_{\mathrm{eq}} = S_{\mathrm{y}}^{\mathrm{h}}$ for $\sigma_{\mathrm{eq}}^{\mathrm{el}} > S_{\mathrm{y}}^{\mathrm{h}} + S_{\mathrm{y}}^{\mathrm{c}}$, $\max\left(\sigma_{\mathrm{eq}}^{\mathrm{el}} - S_{\mathrm{y}}^{\mathrm{c}}, 0.8\ S_{\mathrm{y}}^{\mathrm{h}}\right)$ for $S_{\mathrm{y}}^{\mathrm{h}} < \sigma_{\mathrm{eq}}^{\mathrm{el}} \leq S_{\mathrm{y}}^{\mathrm{h}} + S_{\mathrm{y}}^{\mathrm{c}}$, $\min\left(\sigma_{\mathrm{eq}}^{\mathrm{el}}, 0.8\ S_{\mathrm{y}}^{\mathrm{h}}\right)$ for $\sigma_{\mathrm{eq}}^{\mathrm{el}} \leq S_{\mathrm{y}}^{\mathrm{h}}$	$\Delta\varepsilon_{\mathrm{eq}} = 1.1\ \Delta\varepsilon_{\mathrm{eq}}^{\mathrm{el}}$	n.a.	(ASME CC N-47, Fig. T-1420-1C)	n.a.	n.a.	(Narayanan et al., 1985)
equivalent von Mises stress	equivalent (total) strain range from ASME BPVC-III-1 NH, T-1414	–	–	MRM-type using minimum values for 0.95-percentile	(nominal, design) Basquin and Coffin-Manson	$\mathrm{SF}_{\mathrm{c}} \in \{1.0, 1.5\}$	•	(Fork et al., 2012), method 1 based upon ASME BPVC-III-1 NH
–	n.a.	–	–	experimental creep fatigue interaction data based upon inelastic strain proportions		$\mathrm{SF}_{\mathrm{total}} = 10$	–	(Fork et al., 2012), method 2 based upon experimental creep-fatigue data

maximum principle stress σ_1^{el}	equivalent von Mises strain	–	$\Delta\varepsilon_{\mathrm{eq}} = 1.1\ \Delta\varepsilon_{\mathrm{eq}}^{\mathrm{el}}$	n.a.	n.a.	$\mathrm{SF_c} = 1.5$, $\mathrm{SF_f} = 2.0$ with $D_\mathrm{f} \geq 10\ \%$	•	(Neises et al., 2014)
–	–	–	–	–	n.a.	n.a.	–	(Liao et al., 2014)
n.a.	n.a.	–	–	quadratic Larson-Miller	–	$D_\mathrm{f} \stackrel{!}{=} 10\ \%$	•	(Ortega et al., 2016a)
–	–	–	–	– ($\sigma <$ UTS/3 from ASME BPVC III-1 NH)		–	–	(Rodríguez-Sánchez et al., 2015; Sánchez-González et al., 2017)
n.a.	equivalent von Mises strain	–	–	MRM-type based upon average creep data	Basquin/ Coffin-Manson-type	$\mathrm{SF_f} = 2.0$	–	(Nithyanandam and Pitchumani, 2016)
equivalent von Mises stress from load controlled stress	equivalent von Mises strain	–	n.a.	n.a.	n.a.	n.a.	•	(Conroy et al., 2018a,b)
–	ASME BPVC-III-5	– (σ_{eq} derived from isochronous stress-strain curves at $\Delta\varepsilon_{\mathrm{eq}}$)	ASME BPVC-III-5	(nominal, design) Larson-Miller for 0.95-percentile	(nominal, CSP, nuclear)	$\mathrm{SF_f} \in \{1.5, 2.0\}$/ $\mathrm{SF_f^*} \in \{10, 20\}$	•	(Barua et al., 2019), creep-fatigue design by elastic analysis

Huddleston model	ASME BPVC-III-5	–	–	(nominal)	(nominal, CSP, nuclear)	$\mathrm{SF_c} \in \{1.0, 1.1, 1.5\}$	•	(Barua et al., 2019), creep-fatigue design by inelastic analysis (cf. Frantz et al. (2020))
equivalent von Mises stress	equivalent von Mises strain	n.a.	n.a.	n.a. ($\sigma <$ UTS/3 outside creep-fatigue regime)		n.a.	n.a.	(Conroy et al., 2019a,b)
equivalent von Mises stress	equivalent von Mises strain	$\sigma_{\mathrm{eq}} = \sigma_{\mathrm{eq}}^{\mathrm{el}}$ for $\sigma_{\mathrm{eq}}^{\mathrm{el}} \leq S_{\mathrm{y}}$, σ_{eq} with Neuber's or Glinka-Molski approximation and monotonic stress-strain curve for $S_{\mathrm{y}} < \sigma_{\mathrm{eq}}^{\mathrm{el}}$ and $\sigma_{\mathrm{eq,T}}^{\mathrm{el}} < 2S_{\mathrm{y}}$, σ_{eq} with Neuber's or Glinka-Molski approximation and cyclic stress-strain curve for $\sigma_{\mathrm{eq,T}}^{\mathrm{el}} \geq 2S_{\mathrm{y}}$; analytical stress relaxation model	$\Delta\varepsilon_{\mathrm{eq}} = \Delta\varepsilon_{\mathrm{eq}}^{\mathrm{el}}$ for $\sigma_{\mathrm{eq,T}}^{\mathrm{el}} < 2S_{\mathrm{y}}$, otherwise $\Delta\varepsilon_{\mathrm{eq}}$ from $\Delta\sigma_{\mathrm{eq}}$ (determined with Neuber's or Glinka-Molski approximation and cyclic stress-strain curve)	MRM-type	(Basquin, and) Coffin-Manson	$\mathrm{SF_c} = 1.1$	•	(González-Gómez et al., 2021)
n.a.	n.a.	–	–	MRM-type	n.a.	n.a.	•	(Rao et al., 2021)

Nomenclature

Roman symbols

a	absorptivity [–]
A, B, C	dimensionless coefficients [–]
D	dimensionless coefficient, (accumulated) damage [–]
$\mathbf{e}$	unit (direction) vector [–]
E	Young's modulus $\left[\mathrm{N\ m^{-2} = kg\ m^{-1}\ s^{-2}}\right]$
f	Darcy friction factor, general function [–]
$\dot{g}$	solar irradiation $\left[\mathrm{W\ m^{-2} = kg\ s^{-3}}\right]$
$\mathbf{g}$	gravity vector $\left[\mathrm{m\ s^{-2}}\right]$
J_2	second invariant of deviatoric stress $\left[\mathrm{N^2\ m^{-4} = kg^2\ m^{-2}\ s^{-4}}\right]$
k	turbulent kinetic energy $\left[\mathrm{J\ kg^{-1} = m^2\ s^{-2}}\right]$
K	solid thermal conductivity $\left[\mathrm{W\ m^{-1}\ K^{-1} = kg\ m\ s^{-3}\ K^{-1}}\right]$
$\overline{\overline{K}}$	Reynolds averaged fluid thermal conductivity $\left[\mathrm{W\ m^{-1}\ K^{-1} = kg\ m\ s^{-3}\ K^{-1}}\right]$
n	dimensionless number [–]
N	dimensionless number, cycle number [–]
p	pressure $\left[\mathrm{N\ m^{-2} = kg\ m^{-1}\ s^{-2}}\right]$
$\dot{q}$	heat flux $\left[\mathrm{W\ m^{-2} = kg\ s^{-3}}\right]$
r	radius, radial coordinate [m]
S	material strength $\left[\mathrm{N\ m^{-2} = kg\ m^{-1}\ s^{-2}}\right]$
SF	safety factor [–]
t	time [s]
T	temperature [K]
$\widehat{v}$	Reynolds averaged fluid velocity $\left[\mathrm{m\ s^{-1}}\right]$
$\mathbf{x}$	location vector [m]
z	axial coordinate [m]

Greek symbols

α	coefficient of thermal expansion $\left[\mathrm{K^{-1}}\right]$
ϵ	emissivity [–]

ε	strain $[-]$, turbulent eddy dissipation $\left[\mathrm{J\ kg^{-1}\ s^{-1} = m^2\ s^{-3}}\right]$
$\boldsymbol{\varepsilon}$	strain tensor $[-]$
$\overline{\overline{\mu}}$	Reynolds averaged fluid dynamic viscosity $\left[\mathrm{N\ s\ m^{-2} = kg\ m^{-1}\ s^{-1}}\right]$
ν	Poisson's ratio $[-]$
$\overline{\overline{\rho}}$	Reynolds averaged fluid density $\left[\mathrm{kg\ m^{-3}}\right]$
σ, $\boldsymbol{\sigma}$	stress (tensor) $\left[\mathrm{N\ m^{-2} = kg\ m^{-1}\ s^{-2}}\right]$
φ	circumferential coordinate $[-]$
ω	turbulent eddy frequency $\left[\mathrm{s^{-1}}\right]$

Superscripts

b	bending
c	cold
C	convection
el	elastic
h	hot
i	inner
o	outer
relax	relaxation
R	radiation
T	turbulence
ν	triaxial stress state
$*$, $**$	alternative

Subscripts

abs	absorbed
adm	admissible
Bi	Biot
c	creep
eq	equivalent
eff	effective
f	fatigue

HS	heliostats
i	(outer element, time) index
j	inner element index
m	maximum element index
n	index
Nu	Nusselt
p	pressure
ref	reference
Re	Reynolds
total	total, i.e. accounting for interaction of damage mechanisms
T	thermal
y	yield
1	maximum principal

Abbreviations

AFD	allowable flux density
AI	artificial intelligence
ASME BPVC-III-1 NH	ASME Boiler and Pressure Vessel Code, Section III, Division 1, Subsection NH
ASME BPVC-III-5	ASME Boiler and Pressure Vessel Code, Section III, Division 5
ASTRID©	Advanced Solar Tubular ReceIver Design
CC	Code-Case
CFD	computational fluid dynamics
CHT	conjugate heat transfer
CSP	concentrating solar power
DNI	direct-normal insolation
HTF	heat transfer fluid
MRM	Mendelson-Roberts-Manson
RANS	Reynolds averaged Navier-Stokes
UTS	ultimate tensile strength

1D	one-dimensional
2D	two-dimensional
3D	three-dimensional

References

ASME, 1980. ASME boiler and pressure vessel code. The American Society of Mechanical Engineers, New York.

ASME, 2015. ASME boiler and pressure vessel code. The American Society of Mechanical Engineers, New York.

ASME, 2017. ASME boiler and pressure vessel code. The American Society of Mechanical Engineers, New York.

Babcock and Wilcox Company, 1984. Molten salt receiver subsystem research experiment phase 1 – final report, volume 1 – technical. Technical Report. Sandia National Laboratories. Albuquerque. URL: https://www.osti.gov/servlets/purl/6406078.

Barua, B., Messner, M.C., McMurtrey, M.D., 2019. Comparison and assessment of the creep-fatigue and ratcheting design methods for a reference gen3 molten salt concentrated solar power receiver, in: ASME 2019 Pressure Vessels & Piping Conference, San Antonio. p. V003T03A100. doi:https://doi.org/10.1115/PVP2019-93572.

BDEW, 2020. Künstliche Intelligenz für die Energiewirtschaft. Technical Report. BDEW Bundesverband der Energie- und Wasserwirtschaft. Berlin. URL: https://www.bdew.de/energie/kuenstliche-intelligenz-fuer-die-energiewirtschaft/.

Benoit, H., Spreafico, L., Gauthier, D., Flamant, G., 2016. Review of heat transfer fluids in tube-receivers used in concentrating solar thermal systems: Properties and heat transfer coefficients. Renewable and Sustainable Energy Reviews 55, 298 – 315. URL: http://www.sciencedirect.com/science/article/pii/S1364032115011387, doi:https://doi.org/10.1016/j.rser.2015.10.059.

Berger, X., Buriot, D., Garnier, F., 1984. About the equivalent radiative temperature for clear skies. Solar Energy 32, 725–733. URL: https:

//www.sciencedirect.com/science/article/pii/0038092X84902470, doi:https://doi.org/10.1016/0038-092X(84)90247-0.

Bergmann, T.L., Lavine, A.S., Incropera, F.P., Dewitt, D.P., 2011. Fundamentals of heat and mass transfer. 7th ed., John Wiley & Sons.

Berman, I., Gangadharan, A., Gupta, G., Narayanan, T., 1979. An interim structural design standard for solar energy applications. Technical Report. Sandia National Laboratories. Albuquerque. URL: https://www.osti.gov/biblio/12260659, doi:10.2172/12260659.

Berman, I., Rao, M.S.M., 1983. Sensitivity of estimated tube life to material property variation. ASME Journal of Pressure Vessel Technology 105, 73 – 79. doi:https://doi.org/10.1115/1.3264242.

Boley, B.A., Weiner, J.H., 1960. Theory of thermal stresses. John Wiley & Sons, New York.

Bradshaw, R.W., Goods, S.H., 2001. Corrosion of alloys and metals by molten nitrates. Technical Report. Sandia National Laboratories. Livermore. URL: https://www.osti.gov/biblio/1545803, doi:10.2172/1545803.

Cess, R.D., 1958. A survey of the literature on heat transfer in turbulent tube flow. Technical Report. Westinghouse Research. Pittsburgh.

Chang, C., Li, X., Zhang, Q., 2014. Experimental and numerical study of the heat transfer characteristics in solar thermal absorber tubes with circumferentially non-uniform heat flux. Energy Procedia 49, 305 – 313. URL: http://www.sciencedirect.com/science/article/pii/S1876610214004871, doi:https://doi.org/10.1016/j.egypro.2014.03.033.

Colebrook, C.F., 1939. Turbulent flow in pipes, with particular reference to the transition region between the smooth and rough pipe laws. Journal of the Institution of Civil Engineers 11, 133–156. URL: https:

//doi.org/10.1680/ijoti.1939.13150, doi:10.1680/ijoti.1939.13150, arXiv:https://doi.org/10.1680/ijoti.1939.13150.

Conroy, T., Collins, M.N., Fisher, J., Grimes, R., 2018a. Levelized cost of electricity evaluation of liquid sodium receiver designs through a thermal performance, mechanical reliability, and pressure drop analysis. Solar Energy 166, 472 – 485. URL: http://www.sciencedirect.com/science/article/pii/S0038092X18302123, doi:https://doi.org/10.1016/j.solener.2018.03.003.

Conroy, T., Collins, M.N., Fisher, J., Grimes, R., 2018b. Thermal and mechanical analysis of a sodium-cooled solar receiver operating under a novel heliostat aiming point strategy. Applied Energy 230, 590 – 614. URL: http://www.sciencedirect.com/science/article/pii/S0306261918312832, doi:https://doi.org/10.1016/j.apenergy.2018.08.113.

Conroy, T., Collins, M.N., Fisher, J., Grimes, R., 2018c. Thermo-hydraulic analysis of single phase heat transfer fluids in csp solar receivers. Renewable Energy 129, 150 – 167. URL: http://www.sciencedirect.com/science/article/pii/S0960148118306268, doi:https://doi.org/10.1016/j.renene.2018.05.101.

Conroy, T., Collins, M.N., Grimes, R., 2019a. Integrated optical-thermal-mechanical model for investigations into high temperature sodium receiver operation. Solar Energy 194, 751 – 765. URL: http://www.sciencedirect.com/science/article/pii/S0038092X19310850, doi:https://doi.org/10.1016/j.solener.2019.10.089.

Conroy, T., Collins, M.N., Grimes, R., 2019b. Sodium receiver designs for integration with high temperature power cycles. Energy 187, 115994. URL: http://www.sciencedirect.com/science/article/pii/S0360544219316883, doi:https://doi.org/10.1016/j.energy.2019.115994.

Conroy, T., Collins, M.N., Grimes, R., 2020. A review of steady-state thermal and mechanical modelling on tubular solar receivers. Renewable and Sustainable Energy Reviews 119, 109591. URL: http://www.sciencedirect.com/science/article/pii/S1364032119307993, doi:https://doi.org/10.1016/j.rser.2019.109591.

DIN, 2011a. DIN EN 12952-3: Water-tube boilers and auxiliary installations – Part 3: Design and calculation for pressure parts of the boiler. Beuth Verlag.

DIN, 2011b. DIN EN 12952-4: Water-tube boilers and auxiliary installations – Part 4: In-service boiler life expectancy calculations. Beuth Verlag.

Doupis, D., Wang, C., Carcorze-Soto, J., Chen, Y.M., Maggi, A., Losito, M., Clark, M., 2016. Transient simulation of molten salt central receiver. AIP Conference Proceedings 1734, 030013. URL: https://aip.scitation.org/doi/abs/10.1063/1.4949065, doi:10.1063/1.4949065, arXiv:https://aip.scitation.org/doi/pdf/10.1063/1.4949065.

Downing, S.R., Socie, D.F., 1982. Simple rainflow counting algorithms. International Journal of Fatigue 4, 31–40.

Du, B.C., He, Y.L., Zheng, Z.J., Cheng, Z.D., 2016. Analysis of thermal stress and fatigue fracture for the solar tower molten salt receiver. Applied Thermal Engineering 99, 741 – 750. URL: http://www.sciencedirect.com/science/article/pii/S1359431116300515, doi:https://doi.org/10.1016/j.applthermaleng.2016.01.101.

Dunn, R., Hearps, P., Wright, M.N., 2012. Molten-salt power towers: Newly commercial concentrating solar storage. Proceedings of the IEEE 100, 504–515.

Eslami, M.R., Hetnarski, R.B., Ignaczak, J., Noda, N., Sumi, N., Tanigawa, Y., 2013. Theory of elasticity and thermal stresses: Explanations, problems and solutions. Springer.

Faupel, J., Fischer, F., 1981. Engineering design: A synthesis of stress analysis and material engineering. 2nd ed., John Wiley & Sons.

Flesch, R., Högemann, D., Hackmann, J., Uhlig, R., Schwarzbözl, P., Augsburger, G., Clark, M., 2017. Dynamic modeling of molten salt power towers. AIP Conference Proceedings 1850, 030016. URL: `https://aip.scitation.org/doi/abs/10.1063/1.4984359`, doi:`10.1063/1.4984359`, `arXiv:https://aip.scitation.org/doi/pdf/10.1063/1.4984359`.

Flores, O., Marugán-Cruz, C., Santana, D., García-Villalba, M., 2014. Thermal stresses analysis of a circular tube in a central receiver. Energy Procedia 49, 354 – 362. URL: `http://www.sciencedirect.com/science/article/pii/S1876610214004925`, doi:`https://doi.org/10.1016/j.egypro.2014.03.038`.

Fork, D.K., Fitch, J., Ziaei, S., Jetter, R.I., 2012. Life estimation of pressurized-air solar-thermal receiver tubes. Journal of Solar Energy Engineering 134, 041016. doi:`https://doi.org/10.1115/1.4007686`.

Frantz, C., Binder, M., Busch, K., Ebert, M., AndreasHeinrich, Kaczmarkiewicz, N., Schlögl-Knothe, B., Kunze, T., Schuhbauer, C., Stetka, M., Schwager, C., Spiegel, M., Boura, C.T., Bauer, T., Bonk, A., Eisen, S., Funck, B., 2020. Basic engineering of a high performance molten salt tower receiver system. AIP Conference Proceedings (in press).

Frantz, C., Fritsch, A., Uhlig, R., 2017. Astrid© – advanced solar tubular receiver design: A powerful tool for receiver design and optimization. AIP Conference Proceedings 1850, 030017. URL: `https://aip.scitation.org/doi/abs/10.1063/1.4984360`, doi:`10.1063/1.4984360`, `arXiv:https://aip.scitation.org/doi/pdf/10.1063/1.4984360`.

Fritsch, A., Uhlig, R., Marocco, L., Frantz, C., Flesch, R., Hoffschmidt, B., 2017. A comparison between transient cfd and fem simulations of solar central receiver tubes using molten salt and liquid metals. Solar Energy 155, 259 – 266. URL: http://www.sciencedirect.com/science/article/pii/S0038092X1730525X, doi:https://doi.org/10.1016/j.solener.2017.06.022.

Glinka, G., 1985. Calculation of inelastic notch-tip strain-stress histories under cyclic loading. Engineering Fracture Mechanics 22, 839–854. URL: https://www.sciencedirect.com/science/article/pii/0013794485901122, doi:https://doi.org/10.1016/0013-7944(85)90112-2.

Gnielinski, V., 1976. New equations for heat and mass-transfer in turbulent pipe and channel flow. International Chemical Engineering 16, 359 – 68.

Gnielinski, V., 2013. On heat transfer in tubes. International Journal of Heat and Mass Transfer 63, 134 – 140. URL: http://www.sciencedirect.com/science/article/pii/S0017931013003207, doi:https://doi.org/10.1016/j.ijheatmasstransfer.2013.04.015.

González-Gómez, P., Rodríguez-Sánchez, M., Laporte-Azcué, M., Santana, D., 2021. Calculating molten-salt central-receiver lifetime under creep-fatigue damage. Solar Energy 213, 180 – 197. URL: http://www.sciencedirect.com/science/article/pii/S0038092X20311890, doi:https://doi.org/10.1016/j.solener.2020.11.033.

Goodier, J.N., 1957. Thermal stresses and deformation. Journal of Applied Mechanics 24, 467 – 474.

Grossmann, J.W., Jones, W.B., Veers, P.S., 1989. Evaluation of thermal cycling creep-fatigue damage for a molten salt receiver. Technical Report. Sandia National Laboratories. Albuquerque. URL: https://www.osti.gov/biblio/7170966.

Gärtner, D., Johannsen, K., Ramm, H., 1974. Turbulent heat transfer in a circular tube with circumferentially varying thermal boundary conditions. International Journal of Heat and Mass Transfer 17, 1003 – 1018. URL: http:

//www.sciencedirect.com/science/article/pii/0017931074901823, doi:https://doi.org/10.1016/0017-9310(74)90182-3.

Ho, C.K., Iverson, B.D., 2014. Review of high-temperature central receiver designs for concentrating solar power. Renewable and Sustainable Energy Reviews 29, 835–846. URL: https://www.sciencedirect.com/science/article/pii/S1364032113006394, doi:https://doi.org/10.1016/j.rser.2013.08.099.

Ho, C.K., Mahoney, A.R., Ambrosini, A., Bencomo, M., Hall, A., Lambert, T.N., 2013. Characterization of pyromark 2500 paint for high-temperature solar receivers. Journal of Solar Energy Engineering 136, 014502–1–4. doi:https://doi.org/10.1115/1.4024031.

IRENA, 2019. Global energy transformation: A roadmap to 2050 (2019 edition). International Renewable Energy Agency (IRENA). URL: https://www.irena.org/publications/2019/Apr/Global-energy-transformation-A-roadmap-to-2050-2019Edition.

Irfan, M.A., Chapman, W., 2009. Thermal stresses in radiant tubes due to axial, circumferential and radial temperature distributions. Applied Thermal Engineering 29, 1913 – 1920. URL: http://www.sciencedirect.com/science/article/pii/S1359431108003621, doi:https://doi.org/10.1016/j.applthermaleng.2008.08.021.

Kalnins, A., 2005. Fatigue analysis in pressure vessel design by local strain approach: Methods and software requirements. Journal of Pressure Vessel Technology 128, 2–7. URL: https://doi.org/10.1115/1.2137770, doi:10.1115/1.2137770.

Khanna, S., Singh, S., Kedare, S.B., 2015. Explicit expressions for temperature distribution and deflection in absorber tube of solar parabolic trough concentrator. Solar Energy 114, 289 – 302. URL: http://www.sciencedirect.com/science/article/pii/S0038092X15000596, doi:https://doi.org/10.1016/j.solener.2015.01.044.

Kistler, B.L., 1987. Fatigue analysis of a solar central receiver design using measured weather data. Technical Report. Sandia National Laboratories. Albuquerque. URL: https://www.osti.gov/biblio/6887825, doi:10.2172/6887825.

Kolb, G.J., 2011. An evaluation of possible next-generation high temperature molten-salt power towers. Technical Report. Sandia National Laboratories. Albuquerque. URL: https://www.osti.gov/biblio/1035342, doi:10.2172/1035342.

Laporte-Azcué, M., González-Gómez, P., Rodríguez-Sánchez, M., Santana, D., 2020a. Deflection and stresses in solar central receivers. Solar Energy 195, 355 – 368. URL: http://www.sciencedirect.com/science/article/pii/S0038092X19311673, doi:https://doi.org/10.1016/j.solener.2019.11.066.

Laporte-Azcué, M., González-Gómez, P., Rodríguez-Sánchez, M., Santana, D., 2020b. Exergy analysis of solar central receivers. Solar Energy 207, 957–973. URL: https://www.sciencedirect.com/science/article/pii/S0038092X20307659, doi:https://doi.org/10.1016/j.solener.2020.07.033.

Lee, C.W., 1966. Thermoelastic stresses in thick-walled cylinders under axial temperature gradient. Journal of Applied Mechanics 33, 467 – 469. doi:https://doi.org/10.1115/1.3625078.

Li, X., Kong, W., Wang, Z., Chang, C., Bai, F., 2010. Thermal model and thermodynamic performance of molten salt cavity receiver. Renewable Energy 35, 981–988. URL: https://www.sciencedirect.com/science/article/pii/S0960148109004935, doi:https://doi.org/10.1016/j.renene.2009.11.017.

Liao, Z., Li, X., Xu, C., Chang, C., Wang, Z., 2014. Allowable flux density on a solar central receiver. Renewable Energy 62, 747 – 753. URL: http://www.sciencedirect.com/science/article/pii/S0960148113004606, doi:https://doi.org/10.1016/j.renene.2013.08.044.

Lilliestam, J., Ollier, L., Labordena, M., Pfenninger, S., Thonig, R., 2020. The near- to mid-term outlook for concentrating solar power: mostly cloudy, chance of sun. Energy Sources, Part B: Economics, Planning, and Policy 0, 1–19. URL: https://doi.org/10.1080/15567249.2020.1773580, doi:10.1080/15567249.2020.1773580, arXiv:https://doi.org/10.1080/15567249.2020.1773580.

Logie, W.R., Pye, J.D., Coventry, J., 2018. Thermoelastic stress in concentrating solar receiver tubes: A retrospect on stress analysis methodology, and comparison of salt and sodium. Solar Energy 160, 368 – 379. URL: http://www.sciencedirect.com/science/article/pii/S0038092X17310757, doi:https://doi.org/10.1016/j.solener.2017.12.003.

Mao, J., Tang, D., Bao, S., Luo, L., Gao, Z., 2016. High temperature strength and multiaxial fatigue life assessment of a tubesheet structure. Engineering Failure Analysis 68, 10–21. URL: https://www.sciencedirect.com/science/article/pii/S1350630716303351, doi:https://doi.org/10.1016/j.engfailanal.2016.05.030.

Marugán-Cruz, C., Flores, O., Santana, D., García-Villalba, M., 2016. Heat transfer and thermal stresses in a circular tube with a non-uniform heat flux. International Journal of Heat and Mass Transfer 96, 256 – 266. URL: http://www.sciencedirect.com/science/article/pii/S0017931015311613, doi:https://doi.org/10.1016/j.ijheatmasstransfer.2016.01.035.

Modest, M.F., 2003. Chapter 5 – Radiative exchange between gray, diffuse surfaces, in: Modest, M.F. (Ed.), Radiative Heat Transfer. 2nd ed.. Academic Press, Burlington, pp. 162–197. URL: https://www.sciencedirect.com/

science/article/pii/B9780125031639500060, doi:https://doi.org/10.1016/B978-012503163-9/50006-0.

Moftakhar, A., Buczynski, A., Glinka, G., 1994. Calculation of elasto-plastic strains and stresses in notches under multiaxial loading. International Journal of Fracture 70, 357–373. URL: https://doi.org/10.1007/BF00032453, doi:10.1007/BF00032453.

Montoya, A., Rodríguez-Sánchez, M., López-Puente, J., Santana, D., 2018. Numerical model of solar external receiver tubes: Influence of mechanical boundary conditions and temperature variation in thermoelastic stresses. Solar Energy 174, 912 – 922. URL: http://www.sciencedirect.com/science/article/pii/S0038092X18309629, doi:https://doi.org/10.1016/j.solener.2018.09.068.

Montoya, A., Rodríguez-Sánchez, M., López-Puente, J., Santana, D., 2020. Influence of longitudinal clips in thermal stresses and deflection in solar tubular receivers. Solar Energy 198, 224 – 238. URL: http://www.sciencedirect.com/science/article/pii/S0038092X20300384, doi:https://doi.org/10.1016/j.solener.2020.01.030.

Narayanan, T.V., Rao, M.S.M., Carli, G., 1985. Structural design and life assessment of a molten salt solar receiver. Journal of Solar Energy Engineering 107, 258 – 263. doi:https://doi.org/10.1115/1.3267688.

Neises, T.W., Wagner, M.J., Gray, A.K., 2014. Structural design considerations for tubular power tower receivers operating at 650 $\circ^{\mathrm{C}}$. Technical Report. National Renewable Energy Lab.. Golden. URL: https://www.osti.gov/biblio/1130170/thumbnail.

Nithyanandam, K., Pitchumani, R., 2016. Thermal and structural investigation of tubular supercritical carbon dioxide power tower receivers. Solar Energy 135, 374 – 385. URL: http:

//www.sciencedirect.com/science/article/pii/S0038092X16301426, doi:https://doi.org/10.1016/j.solener.2016.05.039.

Noda, N., Hetnarski, R.B., Tanigawa, Y., 2003. Thermal stresses. 2nd ed., CRC Press, Boca Raton.

Ortega, J., Khivsara, S., Christian, J., Ho, C., Dutta, P., 2016a. Coupled modeling of a directly heated tubular solar receiver for supercritical carbon dioxide brayton cycle: Structural and creep-fatigue evaluation. Applied Thermal Engineering 109, 979 – 987. URL: http://www.sciencedirect.com/science/article/pii/S1359431116309346, doi:https://doi.org/10.1016/j.applthermaleng.2016.06.031. special Issue: Solar Energy Research Institute for India and the United States (SERIIUS) – Concentrated Solar Power.

Ortega, J., Khivsara, S., Christian, J., Ho, C., Yellowhair, J., Dutta, P., 2016b. Coupled modeling of a directly heated tubular solar receiver for supercritical carbon dioxide brayton cycle: Optical and thermal-fluid evaluation. Applied Thermal Engineering 109, 970 – 978. URL: http://www.sciencedirect.com/science/article/pii/S1359431116308572, doi:https://doi.org/10.1016/j.applthermaleng.2016.05.178. special Issue: Solar Energy Research Institute for India and the United States (SERIIUS) – Concentrated Solar Power.

Pacheco, J.E. (Ed.), 2002. Final test and evaluation results from the Solar Two project. Sandia National Laboratories, Albuquerque. URL: https://www.osti.gov/biblio/793226-final-test-evaluation-results-from-solar-two-project.

Petukhov, B., 1970. Heat transfer and friction in turbulent pipe flow with variable physical properties, in: Hartnett, J.P., Irvine, T.F. (Eds.), Advances in heat transfer. Elsevier. volume 6, pp. 503 – 564. URL: http://www.sciencedirect.com/science/article/

pii/S0065271708701539, doi:https://doi.org/10.1016/S0065-2717(08)70153-9.

Pitz-Paal, R., 2020. 19 - concentrating solar power, in: Letcher, T.M. (Ed.), Future Energy (Third Edition). third edition ed.. Elsevier, pp. 413 – 430. URL: http://www.sciencedirect.com/science/article/pii/B9780081028865000190, doi:https://doi.org/10.1016/B978-0-08-102886-5.00019-0.

Qiu, Y., Li, M.J., Li, M.J., Zhang, H.H., Ning, B., 2019. Numerical and experimental study on heat transfer and flow features of representative molten salts for energy applications in turbulent tube flow. International Journal of Heat and Mass Transfer 135, 732 – 745. URL: http://www.sciencedirect.com/science/article/pii/S0017931018346246, doi:https://doi.org/10.1016/j.ijheatmasstransfer.2019.02.004.

Rao, Z., Bao, S., Liu, X., Taylor, R.A., Liao, S., 2021. Estimating allowable energy flux density for the supercritical carbon dioxide solar receiver: A service life approach. Applied Thermal Engineering 182, 116024. URL: http://www.sciencedirect.com/science/article/pii/S1359431120335055, doi:https://doi.org/10.1016/j.applthermaleng.2020.116024.

Rodríguez-Sánchez, M., Marugán-Cruz, C., Acosta-Iborra, A., Santana, D., 2018. Thermo-mechanical modelling of solar central receivers: Effect of incident solar flux resolution. Solar Energy 165, 43 – 54. URL: http://www.sciencedirect.com/science/article/pii/S0038092X18302147, doi:https://doi.org/10.1016/j.solener.2018.03.005.

Rodríguez-Sánchez, M., Sánchez-González, A., Marugán-Cruz, C., Santana, D., 2015. Flow patterns of external solar receivers. Solar Energy 122, 940 – 953. URL: http://www.sciencedirect.com/science/article/pii/

S0038092X15005769, doi:https://doi.org/10.1016/j.solener.2015.10.025.

Rodríguez-Sánchez, M., Soria-Verdugo, A., Almendros-Ibáñez, J.A., Acosta-Iborra, A., Santana, D., 2014a. Thermal design guidelines of solar power towers. Applied Thermal Engineering 63, 428 – 438. URL: http://www.sciencedirect.com/science/article/pii/S1359431113008028, doi:https://doi.org/10.1016/j.applthermaleng.2013.11.014.

Rodríguez-Sánchez, M.R., Marugán-Cruz, C., Acosta-Iborra, A., Santana, D., 2014b. Comparison of simplified heat transfer models and cfd simulations for molten salt external receiver. Applied Thermal Engineering 73, 993 – 1005. URL: http://www.sciencedirect.com/science/article/pii/S1359431114007686, doi:https://doi.org/10.1016/j.applthermaleng.2014.08.072.

Siebers, D.L., Kraabel, J.S., 1984. Estimating convective energy losses from solar central receivers. Technical Report. Sandia National Laboratories. Livermore. doi:10.2172/6906848.

Slemp, W.S., Wade, W.R., 1962. A method for measuring the spectral normal emittance in air of a variety of materials having stable emittance characteristics. Technical Report. National Aeronautics and Space Administration. Hampton.

Smith, D.C., 1992. Design and optimization of tube-type receiver panels for molten salt application. Journal of Solar Energy Engineering 2, 1029 – 1036.

Sánchez-González, A., Rodríguez-Sánchez, M.R., Santana, D., 2017. Aiming strategy model based on allowable flux densities for molten salt central receivers. Solar Energy 157, 1130 – 1144. URL: http://www.sciencedirect.com/science/article/pii/S0038092X16001468, doi:https://doi.org/10.1016/j.solener.2015.12.055.

Sánchez-González, A., Rodríguez-Sánchez, M.R., Santana, D., 2020. Allowable solar flux densities for molten-salt receivers: Input to the aiming strategy. Results in Engineering 5, 100074. URL: http://www.sciencedirect.com/science/article/pii/S259012301930074X, doi:https://doi.org/10.1016/j.rineng.2019.100074.

Timoshenko, S., Goodier, J.N., 1951. Theory of elasticity. McGraw-Hill Book Company.

Uhlig, R., Frantz, C., Flesch, R., Fritsch, A., 2018. Stress analysis of external molten salt receiver. AIP Conference Proceedings 2033, 040040. URL: https://aip.scitation.org/doi/abs/10.1063/1.5067076, doi:10.1063/1.5067076, arXiv:https://aip.scitation.org/doi/pdf/10.1063/1.5067076.

Uhlig, R., Frantz, C., Fritsch, A., 2016. Effects of vertically ribbed surface roughness on the forced convective heat losses in central receiver systems. AIP Conference Proceedings 1734, 030036. URL: https://aip.scitation.org/doi/abs/10.1063/1.4949088, doi:10.1063/1.4949088, arXiv:https://aip.scitation.org/doi/pdf/10.1063/1.4949088.

Vant-Hull, L.L., 2002. The Role of “Allowable Flux Density” in the Design and Operation of Molten-Salt Solar Central Receivers . Journal of Solar Energy Engineering 124, 165–169. URL: https://doi.org/10.1115/1.1464124, doi:10.1115/1.1464124.

Verein Deutscher Ingenieure, VDI-Gesellschaft Verfahrenstechnik und Chemieingenieurwesen (Ed.), 2010. VDI Heat Atlas. 2nd ed., Springer Berlin Heidelberg.

Willner, K., 2003. Kontinuums- und Kontaktmechanik: Synthetische und Analytische Darstellung. Springer.

Xu, L., Stein, W., Kim, J.S., Wang, Z., 2018. Three-dimensional transient numerical model for the thermal performance of the solar receiver. Renewable Energy 120, 550 – 566. URL: http://www.sciencedirect.com/science/article/pii/S0960148117312594, doi:https://doi.org/10.1016/j.renene.2017.12.055.

Yang, K.W., Lee, C.W., 1971. Thermal stresses in thick-walled circular cylinders under axisymmetric temperature distribution. Journal of Engineering for Industry 93, 969 – 975. doi:https://doi.org/10.1115/1.3428091.

Yang, X., Yang, X., Ding, J., Shao, Y., Fan, H., 2012. Numerical simulation study on the heat transfer characteristics of the tube receiver of the solar thermal power tower. Applied Energy 90, 142 – 147. URL: http://www.sciencedirect.com/science/article/pii/S030626191100451X, doi:https://doi.org/10.1016/j.apenergy.2011.07.006.

Ying, Z., He, B., Su, L., Kuang, Y., He, D., Lin, C., 2020. Convective heat transfer of molten salt-based nanofluid in a receiver tube with non-uniform heat flux. Applied Thermal Engineering 181, 115922. URL: http://www.sciencedirect.com/science/article/pii/S1359431120334049, doi:https://doi.org/10.1016/j.applthermaleng.2020.115922.

Young, W., Budynas, R., 2002. Roark's formulas for stress and strain. 7th ed., McGraw-Hill, New York.

Zanino, R., Bonifetto, R., Christian, J., Ho, C., Richard, L.S., 2014. Effects of rans-type turbulence models on the convective heat loss computed by cfd in the solar two power tower. Energy Procedia 49, 569–578. URL: https://www.sciencedirect.com/science/article/pii/S1876610214005153, doi:https://doi.org/10.1016/j.egypro.2014.03.061. proceedings of the SolarPACES 2013 International Conference.

Zavoico, A.B., 2001. Design basis document. Technical Report. Sandia National Laboratories. Albuquerque. URL: https://www.osti.gov/biblio/786629-solar-power-tower-design-basis-document-revision.

Zhang, Q., Li, X., Wang, Z., Zhang, J., El-Hefni, B., Xu, L., 2015. Modeling and simulation of a molten salt cavity receiver with dymola. Energy 93, 1373 – 1384. URL: http://www.sciencedirect.com/science/article/pii/S0360544215013729, doi:https://doi.org/10.1016/j.energy.2015.10.010.